nanomaterials

MDPI

Article

Construction and Performance Characterization of $BiTmFeSbO_7/BiTmO_3$ Heterojunction Photocatalyst and the Photocatalytic Degradation of Sulfathiazole Under Visible Light Irradiation

Jingfei Luan [1,2,*], Xiqi Gou [1], Ye Yao [1], Liang Hao [1] and Minghe Ma [1]

[1] School of Physics, Changchun Normal University, Changchun 130032, China; 15981009457@139.com (X.G.); yaoye1109@mails.jlu.edu.cn (Y.Y.); 19845486007@139.com (L.H.); 13251704137@139.com (M.M.)
[2] State Key Laboratory of Pollution Control and Resource Reuse, School of the Environment, Nanjing University, Nanjing 210093, China
* Correspondence: jfluan@nju.edu.cn; Tel.: +86-199-5193-9498

Abstract

In this study, a novel photocatalytic nanomaterial $BiTmFeSbO_7$ was successfully synthesized for the first time by using the solvothermal method. On account of the effective Z-scheme mechanism, the $BiTmFeSbO_7/BiTmO_3$ heterojunction photocatalyst (BTBTHP) could effectively separate the photoinduced electrons and the photoinduced holes, concurrently, the high oxidation potential and reduction potential of the $BiTmFeSbO_7$ and the $BiTmO_3$ were retained. Additionally, a Z-scheme BTBTHP was synthesized by using an ultrasound-assisted solvothermal approach. As a result, the BTBTHP exhibited excellent photocatalytic performance during the degradation process of the sulfathiazole (STZ). The morphological features, composition distribution, photochemistry properties and photoelectric properties of the prepared samples were investigated by using the comprehensive characterization techniques. Under the condition of visible light irradiation, the BTBTHP demonstrated an excellent removal efficiency of 99.50% for degrading the STZ. Contrastive analysis results indicated that the removal efficiency of the STZ by using the BTBTHP was substantially higher than that by using the $BiTmFeSbO_7$, the $BiTmO_3$, and the N-doped TiO_2. The removal rate of the STZ by using the BTBTHP was 1.14 times that by using the $BiTmFeSbO_7$, 1.28 times that by using the $BiTmO_3$, and 2.71 times that by using the N-doped TiO_2. Moreover, the stability and the reusability of the BTBTHP were verified through five successive photocatalytic cyclic degradation experiments, indicating that the BTBTHP owned potential for the practical application. The active species which was produced by the BTBTHP were identified as hydroxyl radicals (•OH), superoxide anions ($\bullet O_2^-$), and photoinduced holes (h^+) by capturing radicals experiments and electron paramagnetic resonance testing experiments. Therefore, the degradation mechanism and the pathway of the STZ could be more comprehensively elucidated. In summary, this study lays a solid foundation for the development and further research of high efficient Z-scheme heterojunction photocatalysts and offers novel insights into sustainable remediation strategies for the STZ pollution.

Keywords: $BiTmFeSbO_7/BiTmO_3$ heterojunction photocatalyst; Z-scheme; sulfathiazole; visible light irradiation; photocatalytic activity; degradation mechanism

check for updates

Academic Editor: Sónia Carabineiro

Received: 27 October 2025
Revised: 16 November 2025
Accepted: 21 November 2025
Published: 23 November 2025

Citation: Luan, J.; Gou, X.; Yao, Y.; Hao, L.; Ma, M. Construction and Performance Characterization of $BiTmFeSbO_7/BiTmO_3$ Heterojunction Photocatalyst and the Photocatalytic Degradation of Sulfathiazole Under Visible Light Irradiation. *Nanomaterials* **2025**, *15*, 1756. https://doi.org/10.3390/nano15231756

Copyright: © 2025 by the authors. Licensee MDPI, Basel, Switzerland. This article is an open access article distributed under the terms and conditions of the Creative Commons Attribution (CC BY) license (https://creativecommons.org/licenses/by/4.0/).

1. Introduction

Antibiotics are a class of compounds which are produced by microorganisms or synthesized artificially through chemical methods [1]. Antibiotics are used to treat microbial infectious diseases and are widely applied in human healthcare, agriculture, animal husbandry, and aquaculture [2,3]. Sulfonamide antibiotics are prolonged synthetic antibiotics which have been utilized for a long time in history. Sulfonamide antibiotics possess broad-spectrum antibacterial activity, significant therapeutic effects, stable properties, and low cost characteristic; thus, sulfonamide antibiotics have become one of the most extensively applied antibiotics [4]. The sulfathiazole (STZ) is one of the most extensively applied sulfonamide antibiotics and has a high detection rate within the aquatic environments. Notably, the STZ cannot be completely metabolized and absorbed within the human and animal bodies. The unabsorbed STZ enters the environment via wastewater discharge in the form of the parent drug or its metabolites, leading to water resource pollution [5]. Numerous studies indicated that the STZ possessed high stability, biological toxicity, water solubility, and strong migration capability [6]. The high mobility of the STZ facilitates its extensive dispersion through water circulation systems; as a result, the STZ is frequently detected in surface waters [7,8] with a concentration of μg/L level [9,10]. The STZ resists the effective removal by using the conventional wastewater treatment systems due to the anionic character and difficult biodegradation characteristic [11]. The accumulating burden of the STZ progressively heightens the potential risks to the organism, including the acute toxicity and the chronic toxicity; concurrently, the microbiologic population undergoes serious threat [12]. The prolonged existence of the STZ which is obtained in the environment facilitates the STZ for going into the food chain; ultimately, human health and animal health are affected [13]. Therefore, developing an efficient and clean method for removing the residual STZ from water bodies is an urgent problem which should be solved.

Up to now, a variety of traditional treatment methods for the STZ removal have been developed and applied, including membrane treatment, biological treatment, and adsorption treatment. However, these methods all exhibit inherent limitations. In recent years, photocatalytic technology has achieved significant attention due to the advantages such as high efficiency, low operational costs, pollution-free operation, high mineralization rate, and environmental friendliness; thus, photocatalytic technology has been widely applied in the environmental field and energy field [14]. As a new advanced oxidation technology, photocatalytic technology has emerged as an effective method for degrading the target pollutants which derive from wastewater [15,16]. Under the condition of the sunlight irradiation, the semiconductor photocatalysts absorb photons for generating the photoinduced electrons and the photoinduced holes (PEPHs). The photoinduced holes oxidize water or hydroxide ions, and thereby the hydroxyl radicals are formed. Meanwhile, the photoinduced electrons reduce the dissolved oxygen which exists in water, and eventually the superoxide anions are formed. The hydroxyl radicals (•OH) and the superoxide anions ($\bullet O_2^-$) are highly oxidative active radicals, which can effectively oxidize and remove the organic pollutants which are contained in wastewater [17].

As a typical photocatalyst, TiO_2 exhibits responsive properties only under the condition of ultraviolet light irradiation due to the wide band gap energy of 3.2 eV for TiO_2. However, the ultraviolet light merely accounts for 4% of the solar spectrum energy; thus, the practical applications of TiO_2 are significantly restricted [18]. In order to more effectively utilize the visible light energy which accounts for 43% of the solar spectrum energy, it is essential to construct composite photocatalysts which are capable of achieving efficient light absorption. In comparison with single metal oxide catalysts, the composite photocatalysts exhibit superior visible light responsive characteristics and superior photocatalytic performance [19–21]. According to the existing reports, the $A_2B_2O_7$-type

compounds and the ABO_3-type compounds exhibit excellent photocatalytic performance under the condition of visible light irradiation (VLIRN). For instance, Liu et al. utilized the $Bi_2Zr_2O_7$ nanocatalyst under the condition of VLIRN; as a result, the photocatalytic removal efficiency of tetracycline was as high as 81.3% [22]. Researchers who came from Tamil Nadu indicated that the $Sm_2Ti_2O_7$ photocatalyst could efficiently degrade rhodamine B dye within wastewater under the condition of VLIRN [23]. Girish et al. reported that the removal rate of ofloxacin by using the $BiFeO_3$ photocatalyst reached 80% after VLIRN of 180 min [24]. Thirumalairajan et al. reported that the degradation removal rate of rhodamine B and methylene blue by using the $LaFeO_3$ nanocatalyst reached 90.66% and 92.85%, respectively, under the condition of VLIRN [25].

In previous studies, we extensively explored the potential for enhancing the photocatalytic performance of the Bi_2InNbO_7 photocatalyst through structural modification. The Bi_2InNbO_7 was a visible light responsive photocatalyst which possessed a stable pyrochlore structure [26]. We also drew inspiration from previous experiments on how to improve the photocatalytic activity of the TiO_2 photocatalyst by doping elements into the TiO_2 photocatalyst. Cheng et al. synthesized the Fe-doped TiO_2; as a result, the Fe-doped TiO_2 showed significantly enhanced photocatalytic degradation efficiency of terramycin compared with pure TiO_2 [27]. Desire et al. synthesized the Tm-doped TiO_2; obviously, the results demonstrated that the Tm-doped TiO_2 had a higher photocatalytic degradation efficiency of methylene blue compared with the undoped TiO_2 [28]. Chen et al. synthesized the Sb-doped TiO_2; as a result, the Sb-doped TiO_2 exhibited significantly enhanced photocatalytic degradation efficiency of methyl orange in comparison with pure TiO_2 [29]. Zhang et al. prepared the Bi-doped TiO_2; obviously, the results indicated that the Bi-doped TiO_2 possessed enhanced photocatalytic degradation efficiency of phenol compared with the undoped TiO_2 [30]. In conclusion, the abovementioned studies all demonstrate that the addition of the elements such as Fe, Tm, Sb, and Bi can boost the photocatalytic activity of TiO_2. Based on the analysis of the above experimental results, we can replace certain specific elements in Bi_2InNbO_7 for increasing the carrier concentration; thereby, the photocatalytic activity of the doped Bi_2InNbO_7 photocatalyst is higher than that of the Bi_2InNbO_7 photocatalyst. In summary, for the Bi_2InNbO_7 photocatalyst, we, respectively, utilize Tm^{3+}, Fe^{3+}, and Sb^{5+} for replacing Bi^{3+}, In^{3+}, and Nb^{5+}; as a result, the new catalyst $BiTmFeSbO_7$ which possesses enhanced photocatalytic activity is synthesized. Similarly, in accordance with the existing literature, the $BiTbO_3$ had potential photocatalytic activity in the visible light region [31]; subsequently, we used Tm^{3+} to replace Tb^{3+} which belonged to $BiTbO_3$ for synthesizing the new catalyst $BiTmO_3$ which owned enhanced photocatalytic activity. Therefore, the novel photocatalysts $BiTmFeSbO_7$ and $BiTmO_3$ which are designed and synthesized in this paper possess superior photocatalytic activity.

However, the single photocatalyst exhibits a severe recombination phenomenon of the PEPH. In order to address the above issue, the heterojunction photocatalysts have been proposed. The formation of the heterojunctions can increase the separation rate of the PEPH [32], and thereby the photocatalytic activity of the heterojunction photocatalysts may be improved. In comparison with the traditional type-II heterojunction photocatalysts, the Z-scheme heterojunction photocatalysts have attracted more attention due to their superior photocatalytic activity; concurrently, the Z-scheme heterojunction photocatalysts have become the current mainstream heterojunctions [33,34].

The design of the Z-scheme heterojunctions draws inspiration from natural photosynthesis which occurs in the plants. The Z-scheme heterojunction is a type of heterojunction which is composed of distinct reduction centers and oxidation centers which derive from two or more semiconductors. Upon absorbing light energy equal to or greater than their respective band gap energy, two distinct systems are formed [35]. Different from the photo-

catalytic degradation mechanism of organic pollutants by using the traditional composite catalysts, the Z-scheme heterojunction structure enables the photogenerated holes to remain in the valence band of the Z-scheme heterojunction catalyst with a more positive electrochemical potential; simultaneously, the photogenerated electrons are allowed to stay in the conduction band of the Z-scheme heterojunction catalyst with a more negative electrochemical potential. Therefore, the photogenerated electrons possess a stronger reducing ability, and, concurrently, the photogenerated holes possess a stronger oxidizing ability [36–38]. Thus far, the Z-scheme heterojunction photocatalysts have made significant progress in the photocatalytic area. For instance, Mafa et al. successfully fabricated a Z-scheme $ZnMoO_4$/$BiFeWO_6$/rGO ternary composite heterojunction photocatalyst; obviously, the results showed that the $ZnMoO_4$/$BiFeWO_6$/rGO ternary composite heterojunction photocatalyst achieved a removal rate of 98% for degrading the anthraquinone blue 25 after VLIRN of 180 min [39]. Liu et al. successfully synthesized a direct Z-scheme BiOBr/CuI heterojunction photocatalyst; as a result, the BiOBr/CuI heterojunction photocatalyst possessed a high photocatalytic activity for the degradation of the phenol under the condition of VLIRN [40]. In accordance with the analysis of the above experimental results, the construction of the Z-scheme heterojunctions can significantly enhance the photocatalytic activity of the photocatalyst.

According to the above insights, a suitable energy band structure should be designed; thus, we propose a novel direct Z-scheme $BiTmFeSbO_7$/$BiTmO_3$ heterojunction photocatalyst (BTBTHP) for the efficient degradation of the STZ under the condition of VLIRN. The innovative research content of this study is the successful preparation of new visible light responsive $BiTmFeSbO_7$ photocatalysts, the $BiTmO_3$ photocatalyst and the BTBTHP, by using the solvothermal method. This study investigates the photocatalytic degradation efficiency of the STZ by using the BTBTHP, the $BiTmFeSbO_7$ photocatalyst, the $BiTmO_3$ photocatalyst, and the nitrogen-doped TiO_2 (N-T) under the condition of VLIRN. The photocatalytic activity of the BTBTHP, the $BiTmFeSbO_7$ photocatalyst, the $BiTmO_3$ photocatalyst, and the N-T photocatalyst are evaluated. The results showed that the BTBTHP exhibited excellent photocatalytic activity compared with the $BiTmFeSbO_7$ photocatalyst, the $BiTmO_3$ photocatalyst and the nitrogen-doped TiO_2 (N-T); meanwhile, the reusability and the stability of the BTBTHP are verified by accomplishing the cyclic experiments. The crystal structure, morphological characteristics, and optical properties of the BTBTHP are thoroughly investigated; concurrently, the possible direct Z-scheme mechanism of the BTBTHP is verified. This study systematically explores the types of radicals, the reaction mechanisms, and the degradation pathways during the photocatalytic degradation process of the STZ. This research provides important process parameters and a theoretical basis for developing an environmentally friendly photocatalytic reaction system which can degrade the STZ efficiently in pharmaceutical wastewater.

2. Experimental Section

2.1. Materials and Reagents

$Bi(NO_3)_3{\cdot}5H_2O$ (purity 99.0%), $Fe(NO_3)_3{\cdot}9H_2O$ (purity 99.9%), and $NaSbO_3$ (purity 98.0%) were procured from Aladdin Industrial Corporation, Shanghai, China. $Tm(NO_3)_3{\cdot}5H_2O$ (purity 99.9%) was purchased from Merck, Shanghai, China. Ethylenediaminetetraacetic acid (EDTA, $C_{10}H_{16}N_2O_8$, purity 99.99%) and benzoquinone (BQ, $C_6H_4O_2$, purity 99.0%) were obtained from Shanghai Macklin Biochemical Co., Ltd. (Shanghai, China). Absolute ethanol (C_2H_5OH, purity 99.5%), isopropyl alcohol (IPA, C_3H_8O, purity 99.999%), and the pollutant STZ ($C_9H_9N_3O_2S_2$, purity 99.0%) were all sourced from Aladdin Industrial Corporation, Shanghai, China.

2.2. Preparation Method of $BiTmO_3$

In this study, the $BiTmO_3$ photocatalyst was synthesized employing the solvothermal method. In the first instance, isovolumetric precursor solutions of $Bi(NO_3)_3{\cdot}5H_2O$ (0.21 mol/L) and $Tm(NO_3)_3{\cdot}5H_2O$ (0.21 mol/L) were thoroughly mixed and magnetically stirred for 1250 min. Subsequently, the obtained homogeneous precursor mixture was transferred into an autoclave which was furnished with polytetrafluoroethylene at a temperature of 230 °C for 750 min. Then, under the condition of a nitrogen atmosphere, the mixture was heated in a tube furnace at a heating rate of 5 °C/min until the temperature reached 1170 °C, and then the mixture was maintained at this temperature for 1620 min. This procedure effectively produced pure $BiTmO_3$ powder.

2.3. Preparation Method of $BiTmFeSbO_7$

The $BiTmFeSbO_7$ photocatalyst was also synthesized by using the solvothermal technique. The isovolumetric precursor solutions of $Bi(NO_3)_3{\cdot}5H_2O$ (0.21 mol/L), $Tm(NO_3)_3{\cdot}5H_2O$ (0.21 mol/L), $Fe(NO_3)_3{\cdot}9H_2O$ (0.21 mol/L), and $NaSbO_3$ (0.21 mol/L) were mixed. After being thoroughly homogenized and magnetically stirred for 1500 min, the precursor solution mixture was transferred into an autoclave which was lined with polytetrafluoroethylene, heated to 210 °C, and maintained at this temperature for 1250 min. The mixture was then heated in a tube furnace at a heating rate of 8 °C/min until a final temperature of 1180 °C was reached; subsequently, the above mixture was maintained at the temperature of 1180 °C for 1560 min. The pure $BiTmFeSbO_7$ powder was successfully synthesized by the above method.

2.4. Synthesis of Nitrogen-Doped TiO_2

The complete production process of the nitrogen-doped TiO_2 photocatalyst is provided in the Supplementary Materials (Section S1).

2.5. Optimal Ratio of $BiTmFeSbO_7$/$BiTmO_3$ Heterojunction Photocatalyst

The molar ratios of the $BiTmFeSbO_7$ to the $BiTmO_3$ were controlled at 1:3, 1:2, 1:1, 2:1, and 3:1; subsequently, the corresponding composite catalyst samples were denoted as BTBTHP-(1:3), BTBTHP-(1:2), BTBTHP, BTBTHP-(2:1), and BTBTHP-(3:1), respectively. Table S1 displays the removal rates of the STZ by using the BTBTHP which possesses different proportions during the photocatalytic degradation process of the STZ under the condition of VLIRN. As summarized in Table S1, the experiments for degrading the STZ under the condition of VLIRN yielded the following results: when the BTBTHP which possessed the molar ratio of 1:1 for the $BiTmFeSbO_7$ to the $BiTmO_3$ was utilized for degrading the STZ, the degradation efficiency of the STZ reached 99.5%, whereas the removal rates of the STZ by using other composite catalysts which owned other molar ratios of the $BiTmFeSbO_7$ to the $BiTmO_3$ were below 90%. The above results indicated that the heterojunction photocatalyst which was prepared with a molar ratio of 1:1 for the $BiTmFeSbO_7$ to the $BiTmO_3$ facilitated the formation of the largest heterojunction catalyst interface, and thereby the separation efficiency of the PEPH was accelerated; ultimately, the strongest photocatalytic activity of the BTBTHP was realized. When the molar ratio of the $BiTmFeSbO_7$ to the $BiTmO_3$ is less than 1, the formed heterojunction catalyst interface is relatively small; as a result, the weak photocatalytic activity of the heterojunction catalyst was realized. Conversely, when the molar ratio of the $BiTmFeSbO_7$ to the $BiTmO_3$ for the heterojunction catalyst exceeds 1, the excessive nanoparticles occupy the active sites which derive from the surface of the heterojunction catalyst; similarly, a relatively low removal rate of the STZ was obtained during the photocatalytic degradation process of the STZ by using the heterojunction catalyst which owned a molar ratio of 2:1 or 3:1 for

the $BiTmFeSbO_7$ to the $BiTmO_3$. In summary, the optimal molar ratio of $BiTmFeSbO_7$ to the $BiTmO_3$ for producing the BTBTHP is 1:1. The heterojunction composite catalyst BTBTHP which was formed in accordance with a molar ratio of 1:1 for $BiTmFeSbO_7$ to the $BiTmO_3$ was utilized in both the photocatalytic performance characterization and the STZ degradation experiments throughout this study.

2.6. Synthesis of $BiTmFeSbO_7$/$BiTmO_3$ Heterojunction Photocatalyst

In this study, the ultrasonic-assisted solvothermal method was used to synthesize BTBTHP. Initially, equal mole numbers of the $BiTmO_3$ photocatalyst and the $BiTmFeSbO_7$ photocatalyst which were previously synthesized by using the solvothermal method were mixed with octanol. The mixture was then sonicated in an ultrasonic bath for 60 min. In order to promote the surface binding of $BiTmO_3$ nanoparticles and $BiTmFeSbO_7$ nanoparticles, the mixture was vigorously stirred at 180 °C for 200 min, and thus the $BiTmFeSbO_7$/$BiTmO_3$ heterostructural catalyst was formed. The centrifugal separation technique was employed to obtain the product once the centrifugal product had cooled to room temperature. The obtained product was washed with ethanol multiple times to ensure complete purification. As to the subsequent usage, the purified powder was placed in a desiccator after being dried for 360 min at 60 °C in a vacuum oven. Eventually, the BTBTHP was successfully prepared.

Furthermore, in accordance with the above-described preparation method, the estimated costs of the N-T, the $BiTmFeSbO_7$, the $BiTmO_3$, and the BTBTHP were approximately USD 353.5 per 100 g, USD 54.3 per 100 g, USD 77.8 per 100 g, and USD 63.4 per 100 g, respectively. It was evident that the cost of the N-T was 6.5 times higher than that of the $BiTmFeSbO_7$, 4.5 times higher than that of the $BiTmO_3$, and 5.6 times higher than that of the BTBTHP.

2.7. Characterization

The descriptions of the characterization details are reported in the Supplementary Materials (Section S2).

2.8. Photoelectrochemical Experiments

The electrochemical impedance spectroscopy (EIS) experiment was conducted on a CHI660D electrochemical workstation which derived from Chenhua Instrument Co., Ltd., Shanghai, China. The working electrode, counter electrode, and reference electrode constituted the standard three-electrode system of this experiment. In the experiment, the Ag/AgCl electrode was utilized as the reference electrode, and, simultaneously, a platinum plate served as the counter electrode; eventually, the prepared catalyst was used as the working electrode. An aqueous solution of 0.5 mol/L Na_2SO_4 with a pH value of 7 was used as the electrolyte. The light source which was utilized during the process of the experiment was composed of a 500 W xenon lamp and a 420 nm cutoff filter.

2.9. Experimental Setup and Procedure

A set of 12 quartz tubes was utilized for each experiment, and each quartz tube contained 40 mL of the reaction solution. As to the STZ solution, the total reaction volume was 480 mL. The photodegradation experiments were performed using a dosage of 0.5 g/L nanocatalyst such as $BiTmFeSbO_7$, $BiTmO_3$, or BTBTHP. The initial concentration of STZ in the pharmaceutical wastewater solution was 0.032mmol/L. The degradation experiments were carried out in a photocatalytic reactor (CEL-LB70, China Educational Jinguang Technology Co., Ltd., Beijing, China). In order to promote the uniform dispersion of the photocatalytic samples throughout the photocatalytic reaction system and reach the

adsorption saturation of the STZ, a dark adsorption process which lasted for 45 min was accomplished in darkness.

During the photocatalytic degradation process, the STZ, a xenon lamp (500 W), and a cut-off filter (420 nm) were used to simulate the effect of VLIRN. Five milliliters of the reaction solution samples were taken out for examination at 15 min intervals during the photocatalytic reaction process. Each sample was then centrifuged for 10 min at 7200 rpm to extract the clear liquid, which was used for additional investigation and analysis. The residual concentration of the STZ was determined by using an Agilent 200 high-performance liquid chromatography (HPLC) system (Agilent Technologies, Palo Alto, CA, USA) by injecting a volume of 10 μL into the HPLC at a flow rate of 1 mL/min for analysis.

The mineralization outcomes of the STZ in the reaction solution were analyzed by using a TOC analyzer (TOC-5000 A, Shimadzu Corporation, Kyoto, Japan). Potassium phthalate ($KHC_8H_4O_4$) was used as the reference substance for measuring the concentration of TOC during the photocatalytic degradation process of the STZ. The potassium phthalate served as the calibration standard. Concurrently, the carbon concentration range was established from 0 mg/L to 100 mg/L.

A calibration study of intermediate products which were produced during the photocatalytic degradation process of the STZ was conducted by using liquid chromatography–mass spectrometry (LC–MS) with a Thermo Quest LCQ Duo system (Thermo Fisher Scientific Corporation, Waltham, MA, USA) and a Beta basic-C18 high-performance liquid chromatography column (Thermo Fisher Scientific Corporation, Waltham, MA, USA). The mobile phase which existed in the LC–MS apparatus consisted of a mixture of 60% methanol and 40% ultrapure water. When the photocatalytic reaction for degrading the STZ stopped, 20 μL of the solution which was generated during the photocatalytic degradation process of the STZ was automatically injected into the LC–MS equipment. In order to identify the intermediate products easily, the range for the mass-to-charge ratio of m/z was established from 50 to 500.

3. Results and Discussion

3.1. Characterization of Photocatalysts

3.1.1. Analysis of Morphological and Structural Characterization

Figure 1a presents the XRD patterns of BTBTHP, $BiTmFeSbO_7$, and $BiTmO_3$. The diffractive peaks and the crystal plane indices which were observed in the XRD pattern of BTBTHP were consistent with that of $BiTmFeSbO_7$ and that of $BiTmO_3$, confirming that the BTBTHP was successfully synthesized. Figure S1 presents the XRD pattern of the $BiTmO_3$ photocatalyst. As shown in Figure S1, the $BiTmO_3$ sample corresponded to the JCPDS card number PDF#04-009-5546. Figure S2 displays the XRD pattern of the $BiTmFeSbO_7$ photocatalyst. As shown in Figure S2, the $BiTmFeSbO_7$ sample corresponded to the JCPDS card number PDF#73-0444. Figure S3a shows the XRD pattern and the Rietveld refinement results of $BiTmFeSbO_7$. Figure S3b indicates the atomic structure of $BiTmFeSbO_7$. Figure S4a displays the XRD pattern and the Rietveld refinement results of $BiTmO_3$. Figure S4b indicates the atomic structure of $BiTmO_3$. In order to obtain the photophysical parameters and crystal structure parameters of $BiTmFeSbO_7$ and $BiTmO_3$, the XRD data of $BiTmFeSbO_7$ and $BiTmO_3$ were refined by the Rietveld method using the Materials Studio 2020, as shown in Figures S3a and S4a, respectively. In accordance with Figure S3a, the precise results of $BiTmFeSbO_7$ which achieved an R_P factor of 4.49%, indicated a significant consistency between the experimental intensities of the diffractive peaks for $BiTmFeSbO_7$ and the theoretical intensities of the diffractive peaks for $BiTmFeSbO_7$. Based on Figure S4a, the precise results of $BiTmO_3$ which achieved an R_P factor of 6.73% illustrated a significant consistency between the experimental intensities of the diffractive peaks for $BiTmO_3$ and the theoretical intensities of the diffractive peaks for $BiTmO_3$. These findings confirm that

the $BiTmFeSbO_7$ photocatalyst possesses the pyrochlore-type structure, while the $BiTmO_3$ photocatalyst has the fluorite structure. Furthermore, the $BiTmFeSbO_7$ photocatalyst and the $BiTmO_3$ photocatalyst exhibit a single pure phase. $BiTmFeSbO_7$ crystallized in the cubic crystal system with the space group of Fd3m, while $BiTmO_3$ crystallized in the cubic crystal system with the space group of Fm3m. The lattice constant of $BiTmFeSbO_7$ was determined to be 10.563 Å; concurrently, the lattice constant of $BiTmO_3$ was confirmed to be 5.396 Å. The crystal structures of the $BiTmFeSbO_7$ photocatalyst and the $BiTmO_3$ photocatalyst were constructed by using the relevant atomic coordinates, crystal systems, lattice constants, structural parameters, and space groups. In addition, Table S2 presents the atomic coordinates and structural parameters of $BiTmFeSbO_7$. Table S3 represents the atomic coordinates and structural parameters of the $BiTmO_3$ photocatalyst. The above conclusions demonstrate the structural stability of the synthetic $BiTmFeSbO_7$ photocatalyst and the $BiTmO_3$ photocatalyst. Simultaneously, the $BiTmFeSbO_7$ photocatalyst and the $BiTmO_3$ photocatalyst highlight the application potential in the water environmental field as efficient photocatalysts.

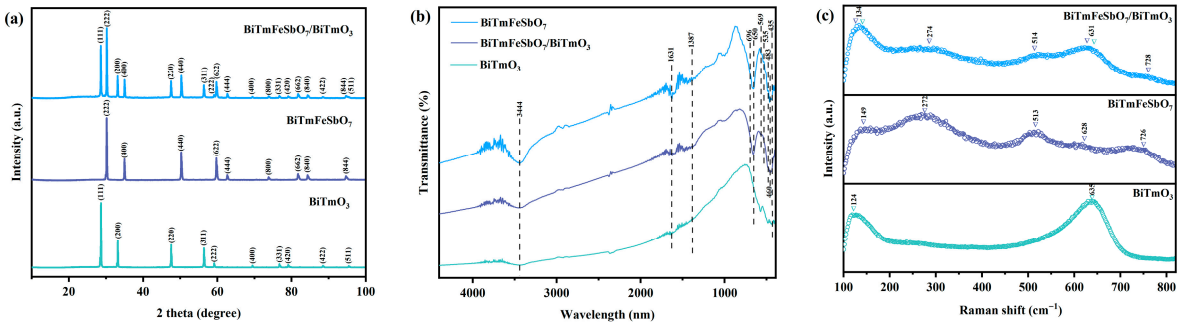


Figure 1. (**a**) The XRD spectra, (**b**) the FTIR spectra, and (**c**) the Raman spectra of the BTBTHP, the $BiTmFeSbO_7$ photocatalyst, and the $BiTmO_3$ photocatalyst.

The unique crystal structure of the $BiTmFeSbO_7$ photocatalyst consists of MO_6 (M = Fe^{3+} and Sb^{5+}) octahedra which are interconnected by Bi^{3+} and Tm^{3+}. In $BiTmFeSbO_7$, there are two types of A-O bonds (A = Bi^{3+} and Tm^{3+}), with the longer A–O(1) bond length of 2.487 Å and the shorter A–O(2) bond length of 2.165 Å. The difference in bond length is expected to cause the distortion of MO_6 octahedra; as a result, the recombination rate of the PEPH decreases [41]. In the crystal structure of $BiTmFeSbO_7$, the M-O-M bond angle was measured to be 134.02°. Previous studies had demonstrated that the photocatalytic activity of the photocatalyst increased when the bond angle of the photocatalyst approached 180° [41]. The larger M-O-M bond angle which belongs to the $BiTmFeSbO_7$ photocatalyst further enhances the photocatalytic activity of $BiTmFeSbO_7$. These findings suggest that the outstanding photocatalytic performance of $BiTmFeSbO_7$ can be ascribed to the unique crystal structure of $BiTmFeSbO_7$. Meanwhile, the above results also indicate the stability of the sample structure for $BiTmFeSbO_7$. Simultaneously, it is emphasized that a thorough understanding of the crystallography for the $BiTmFeSbO_7$ photocatalyst is crucial for optimizing the photocatalytic activity of the $BiTmFeSbO_7$ photocatalyst.

Figure S5 displays the XRD pattern of the nitrogen-doped titanium dioxide. In accordance with Figure S5, the XRD pattern of the nitrogen-doped titanium dioxide revealed that the sample exhibited characteristic crystal planes of the anatase titanium dioxide (JCPDS No. 21-1272).

In order to analyze the functional groups and chemical bonds which belonged to the BTBTHP, the $BiTmFeSbO_7$ photocatalyst, and the $BiTmO_3$ photocatalyst, the Fourier transform infrared (FTIR) spectrogram analysis was performed by using the FTIR spectrometer (Beijing North Finray Analytical Instrument Co., Ltd., Beijing, China). Figure 1b displays

the FTIR spectra of the $BiTmFeSbO_7$ photocatalyst, the BTBTHP, and the $BiTmO_3$ photocatalyst. As shown in Figure 1b, the FTIR spectra exhibited several characteristic absorption peaks, which were associated with the Bi-O bond, Tm-O bond, Fe-O bond, Sb-O bond, and Sb-O-Sb bond. The stretching vibration of the Bi-O bond occurred at 435 cm^{-1} [42,43], while the bending vibration of the Tm-O bond was observed at 650 cm^{-1} [44]. The stretching vibration of the Fe-O bond was related to the peak at 483 cm^{-1} or 535 cm^{-1} [45]; nevertheless, the bending vibration of the Sb-O bond was observed at 460 cm^{-1} [46]. The bending vibration of the Sb-O-Sb bond was detected at 569 cm^{-1} and 696 cm^{-1} [47]. A broad band which was centered at 3444 cm^{-1} indicated the stretching vibration mode of the hydroxyl group which was adsorbed by water [48,49]. Equally, the broad band which was detected at 1631 cm^{-1} corresponded to the bending vibration of hydroxyl groups which existed on the surface of the catalyst [50]. Furthermore, the absorption peak which existed at approximately 1387 cm^{-1} was attributed to the OH vibration of water molecules which were adsorbed on the sample surface [51].

The molecular structures of the $BiTmO_3$ photocatalyst, the $BiTmFeSbO_7$ photocatalyst, and the BTBTHP were investigated by using the Raman spectroscopy for probing their characteristic chemical bond vibrations. Figure 1c displays the Raman spectra of the $BiTmFeSbO_7$ photocatalyst, the $BiTmO_3$ photocatalyst, and the BTBTHP. In the Raman spectrum of the $BiTmFeSbO_7$ photocatalyst, the peak which was observed at 149 cm^{-1} corresponded to the Fg mode and Ag mode of the Tm-O bond [52]. The peak which was observed at 272 cm^{-1} was attributed to the stretching vibration mode of the Bi-O bond [53]. The peak located at 513 cm^{-1} was associated with the A_{1g} bending vibration mode of the O-M-O bond in the MO_6 (M = Fe^{3+} and Sb^{5+}) octahedra [54]. The peak located at 628 cm^{-1} could be attributed to the combined modes of A_{1g} and F_{2g} [54,55]. Additionally, the peak located at 726 cm^{-1} was related to the F_{2g} stretching vibration mode of the M-O bond and the O-M-O bond which existed in the MO_6 octahedra [54,56]. In the Raman spectrum of the $BiTmO_3$ photocatalyst, the peak located at 124 cm^{-1} was attributed to the stretching vibration mode of the Bi-O bond [57], while the peak located at 639 cm^{-1} corresponded to the F_g mode and the A_g mode of the Tm-O bond [58]. Additionally, the Raman spectrum of the BTBTHP included the different absorption peaks derived from the $BiTmFeSbO_7$ photocatalyst and the $BiTmO_3$ photocatalyst. Therefore, the BTBTHP possessed peaks which were located at 134 cm^{-1}, 274 cm^{-1}, 514 cm^{-1}, 631 cm^{-1}, and 728 cm^{-1}. These results provide indirect evidence for the successful preparation of the $BiTmO_3$ photocatalyst, the $BiTmFeSbO_7$ photocatalyst, and the BTBTHP. Additionally, Figures S6–S8 show the Raman spectra of the $BiTmO_3$ photocatalyst, the $BiTmFeSbO_7$ photocatalyst, and the BTBTHP, respectively.

The microstructure of the BTBTHP was investigated by using the transmission electron microscopy (TEM); simultaneously, the elemental composition content and the elemental qualitative judgment of the BTBTHP were determined by using the energy dispersive X-ray spectrometer (EDS) (Thermo Fisher Scientific, Waltham, MA, USA). Figure 2a displays the TEM morphology image of the BTBTHP. Figure 2b displays the high-resolution transmission electron microscopy (HRTEM) image of the BTBTHP. In order to better reveal the microstructure of the BTBTHP composite sample, two additional TEM and HRTEM images have been provided, as shown in Figures S9 and S10. Figure 3 shows the EDS elemental scanning map of the BTBTHP. It can be found from Figure 2a that the TEM morphology image of the BTBTHP explicitly described the presence of the $BiTmFeSbO_7$ nanoparticle and the $BiTmO_3$ nanoparticle which belonged to the BTBTHP. Additionally, the HRTEM stripe image of the interface between the $BiTmFeSbO_7$ nanoparticle and the $BiTmO_3$ nanoparticle which were marked in Figure 2a can be found from Figure 2b. As a result, the lattice plane spacing d value of 0.305 nm corresponded to the crystal plane index of (222) for the

$BiTmFeSbO_7$ photocatalyst, and the lattice plane spacing d value of 0.312 nm corresponded to the crystal plane index of (111) for the $BiTmO_3$ photocatalyst. The close interfacial contact between the $BiTmFeSbO_7$ photocatalyst and the $BiTmO_3$ photocatalyst was emphasized, clearly confirming that the coexistence of the $BiTmFeSbO_7$ photocatalyst and the $BiTmO_3$ photocatalyst was realized in the prepared heterojunction catalyst BTBTHP. The results presented in Figure 3 indicated that the larger particles contained Bi element, Tm element, Fe element, Sb element, and O element. Conversely, the smaller particles did not contain Fe element and Sb element; however, the smaller particles contained Bi element, Tm element, and O element. In accordance with the above analysis, we could draw a conclusion that the larger particles corresponded to the $BiTmFeSbO_7$ photocatalyst while the smaller particles corresponded to the $BiTmO_3$ photocatalyst. Additionally, Figure 4 displays the EDS spectrum of the BTBTHP. The EDS spectrum which is shown in Figure 4 indicated that the atomic ratio of the Bi element, Tm element, Fe element, Sb element, and O element which were contained in the BTBTHP was approximately 1235:1362:611:613:6179. Based on the above comprehensive results, it could be convincingly concluded that the high-purity BTBTHP was successfully synthesized under the specified preparation parameters.

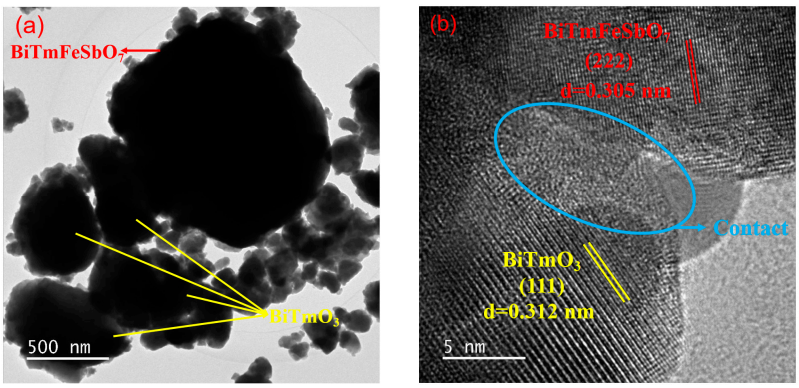


Figure 2. (**a**) The TEM morphology image of the BTBTHP and (**b**) the HRTEM image of the BTBTHP.

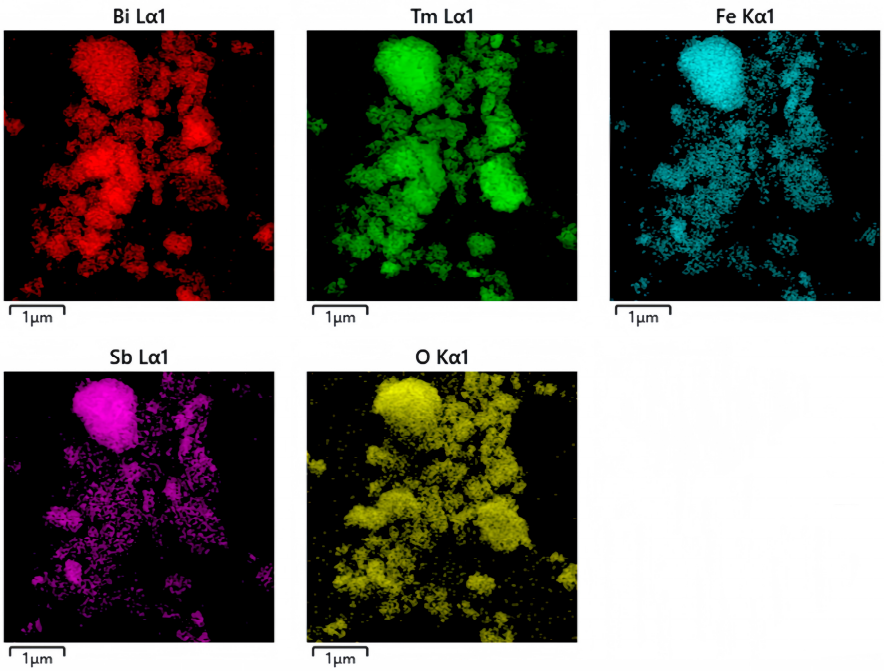


Figure 3. The EDS element scanning mapping of the BTBTHP (Bi, Tm, Fe, Sb, and O from $BiTmFeSbO_7$; simultaneously, Bi, Tm, and O from $BiTmO_3$).

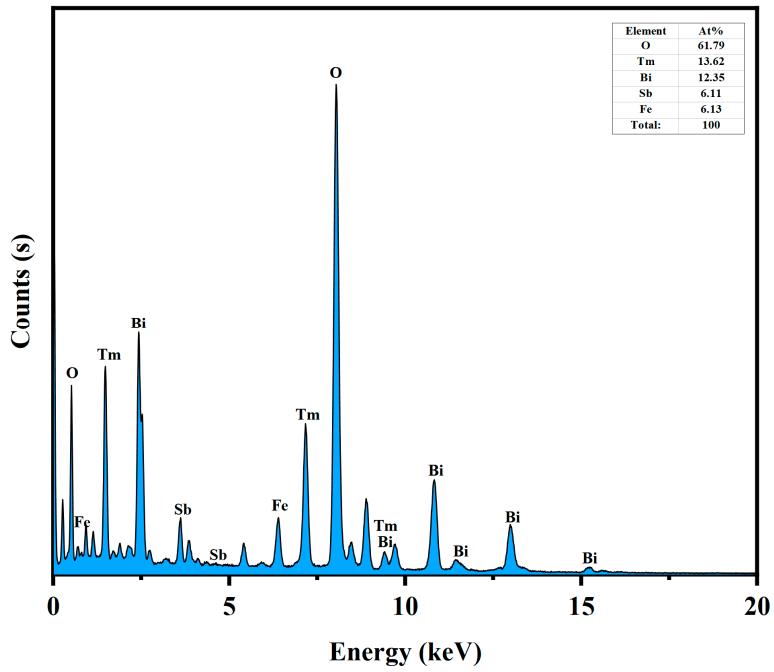


Figure 4. The EDS spectrum of the BTBTHP.

The X-ray photoelectron spectrometer (XPS) (VersaProbe, UlVAC-PHI, Chigasaki, Japan) was used for assessing the chemical composition content and oxidation states of the BTBTHP, the $BiTmFeSbO_7$ photocatalyst, and the $BiTmO_3$ photocatalyst. Figure 5 illustrates the XPS spectra of the $BiTmFeSbO_7$ photocatalyst, the BTBTHP, and the $BiTmO_3$ photocatalyst. Figure 5a indicates the XPS survey spectra of the $BiTmFeSbO_7$ photocatalyst, the BTBTHP, and the $BiTmO_3$ photocatalyst. The XPS spectra for the BTBTHP which is presented in Figure 5a revealed the presence of Bi element, Tm element, Fe element, Sb element, and O element, with the carbon peak serving as a calibration reference. Moreover, the XPS spectrum of the $BiTmO_3$ photocatalyst was compared with that of the BTBTHP; accordingly, a distinct iron signal and antimony signal were detected in the XPS spectrum of the BTBTHP, indicating that the BTBTHP encompassed the single-phase $BiTmFeSbO_7$.

Figure 5b shows the XPS spectral peaks of Bi $4f_{7/2}$ and Bi $4f_{5/2}$ which belong to the $BiTmFeSbO_7$ photocatalyst, the $BiTmO_3$ photocatalyst, and the BTBTHP. As shown in Figure 5b, the Bi $4f_{7/2}$ peak and the Bi $4f_{5/2}$ peak of $BiTmFeSbO_7$ were positioned at 159.43 eV and 164.65 eV, respectively, while the Bi $4f_{7/2}$ peak and the Bi $4f_{5/2}$ peak of the $BiTmO_3$ photocatalyst were located at 160.05 eV and 165.27 eV, respectively. The spin–orbit splitting value was 5.22 eV for the above two cases, which was consistent with the +3 oxidation state of the Bi element [59–61]. In the BTBTHP, the Bi $4f_{7/2}$ peak and the Bi $4f_{5/2}$ peak exhibited a slight shift to 159.75 eV and 164.97 eV.

Figure 5c displays the XPS spectral peak of Tm $4d_{5/2}$ which belongs to the $BiTmFeSbO_7$ photocatalyst, the $BiTmO_3$ photocatalyst, and the BTBTHP. In Figure 5c, the $4d_{5/2}$ peak of Tm derived from the $BiTmFeSbO_7$ photocatalyst was located at 176.81 eV and the $4d_{5/2}$ peak of Tm which originated from the $BiTmO_3$ photocatalyst was located at 177.79 eV. Simultaneously, the $4d_{5/2}$ peak of Tm which originated from the BTBTHP shifted to 177.42 eV. In accordance with Figure 5c, the +3 oxidation state was obtained for the Tm element.

Figure 5d indicates the XPS spectral peaks of Fe $2p_{1/2}$ and Fe $2p_{3/2}$ which belong to the $BiTmFeSbO_7$ photocatalyst and the BTBTHP. Figure 5d demonstrated that the Fe $2p_{1/2}$ peak and the Fe $2p_{3/2}$ peak of the $BiTmFeSbO_7$ photocatalyst were located at 723.94 eV and 710.73 eV. As a result, the spin–orbit splitting value which was calculated according to the above 723.94 eV and 710.73 eV was 13.21 eV, indicating that the +3 oxidation state was

obtained for the Fe element [59–61]. In the BTBTHP, the Fe $2p_{1/2}$ peak and the Fe $2p_{3/2}$ peak shifted slightly to 724.19 eV and 710.98 eV, individually.

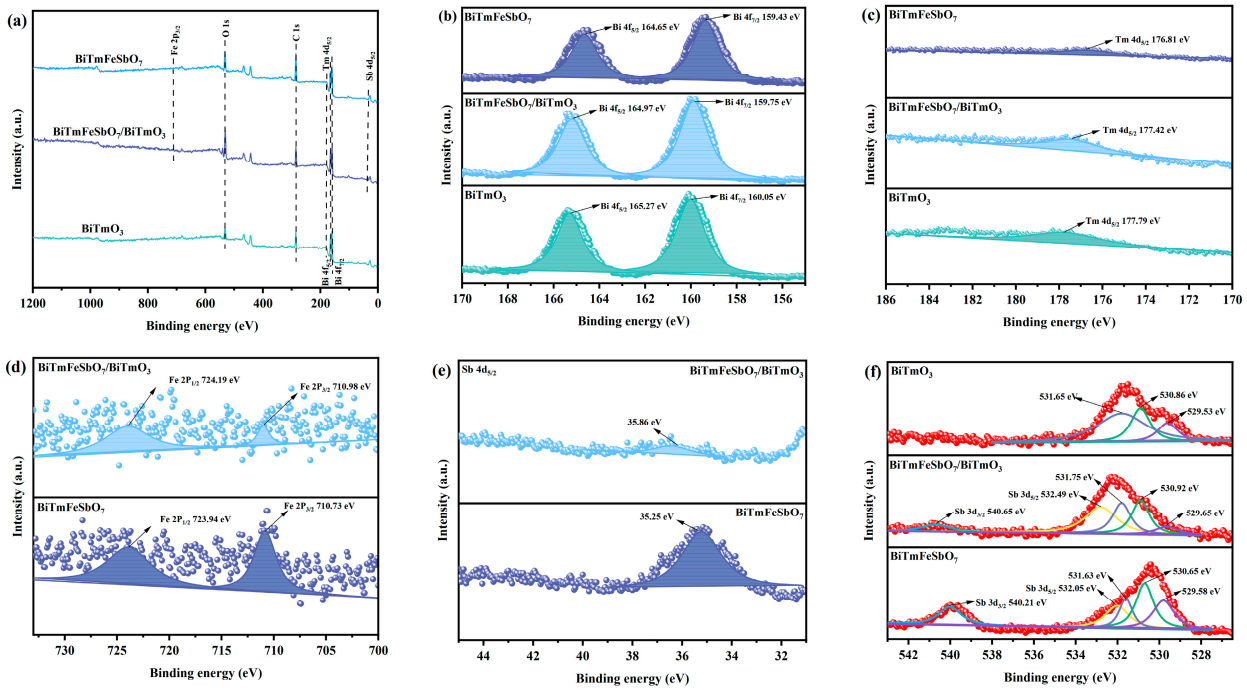


Figure 5. The XPS spectra of the synthesized $BiTmFeSbO_7$ photocatalyst, the $BiTmO_3$ photocatalyst, and the BTBTHP: (**a**) survey spectrum, (**b**–**f**) high-resolution spectra of Bi 4f, Tm 4d, Fe 2p, Sb 4d, Sb 3d, and O 1S.

Figure 5e illustrates the XPS spectral peak of Sb $4d_{5/2}$ which belongs to the $BiTmFeSbO_7$ photocatalyst and the BTBTHP. Figure 5e depicts that the $4d_{5/2}$ peak of Sb derived from the $BiTmFeSbO_7$ photocatalyst was located at 35.25 eV; concurrently, the $4d_{5/2}$ peak of Sb which came from the BTBTHP underwent a shift to 35.86 eV. According to Figure 5e, the +5 oxidation state was obtained for the Sb element.

Figure 5f exhibits the XPS spectral peaks of Sb $3d_{5/2}$ and O 1s which belong to the $BiTmFeSbO_7$ photocatalyst, the $BiTmO_3$ photocatalyst, and the BTBTHP. Figure 5f demonstrated that the Sb $3d_{3/2}$ peak and the Sb $3d_{5/2}$ peak of the $BiTmFeSbO_7$ photocatalyst were located at 540.21 eV and 532.05 eV, respectively; meanwhile, the Sb $3d_{3/2}$ peak and the Sb $3d_{5/2}$ peak of the BTBTHP were positioned at 540.65 eV and 532.75 eV, respectively. It can be found from Figure 5f that the deconvoluted O 1s spectra of the BTBTHP, the $BiTmFeSbO_7$ photocatalyst, and the $BiTmO_3$ photocatalyst were achieved. In accordance with Figure 5f, the peaks which were observed at 529.65 eV, 529.53 eV, and 529.58 eV were attributable to lattice oxygen [62]. Furthermore, the peaks which were observed at 530.92 eV, 530.86 eV, and 530.65 eV signified the signal which stemmed from adsorbed oxygen [62]. Ultimately, the peaks which were observed at 531.75 eV, 531.65 eV, and 531.63 eV indicated the existence of surface hydroxyl groups [63]. In the light of Figure 5f, the -2 oxidation state was obtained for the oxygen element.

The binding energy of the Bi 4f peak, Tm 4d peak, Fe 2p peak, Sb 4d peak, and Sb 3d peak which existed in the BTBTHP exhibited a positive shift in comparison with that in the $BiTmFeSbO_7$ photocatalyst. However, the binding energy of the Bi 4f peak and the Tm 4d peak which existed in the BTBTHP displayed a negative shift compared with that in the $BiTmO_3$ photocatalyst, indicating that there was a significant change for the electron density within the heterojunction [64]. Specifically, the above changes indicated that the electron density of Fe and Sb which derived from the BTBTHP decreased; concurrently,

the electron density of some Bi and some Tm which came from the BTBTHP increased. Inversely, the electron density of other Bi and other Tm which originated from the BTBTHP decreased [64]. The above phenomenon clearly demonstrates the successful hybridization of the $BiTmFeSbO_7$ photocatalyst and the $BiTmO_3$ photocatalyst; thereby, the formation of the BTBTHP is validated. The research results further reveal that the intricate electronic interaction mechanism exists inside the BTBTHP. As a result, this interaction is pivotal for enhancing the functional properties of the BTBTHP.

Notably, in accordance with the XPS analysis results, the peak signals which correspond to other secondary phases are not detected in the BTBTHP sample, the $BiTmFeSbO_7$ sample, and the $BiTmO_3$ sample. Overall, these XPS findings further corroborate the strong chemical interaction between the $BiTmFeSbO_7$ photocatalyst and the $BiTmO_3$ photocatalyst. These XPS results are consistent with those detection results which are obtained from multiple characterization spectra, including the XRD patterns, the FTIR spectra, the Raman spectra, the TEM morphology image, the HRTEM image, and the EDS element scanning mapping. Eventually, the above detection results collectively verify the compositional characteristic and structural characteristic of the BTBTHP, the $BiTmFeSbO_7$ photocatalyst, and the $BiTmO_3$ photocatalyst.

3.1.2. Optical Characteristics

Figure 6a illustrates the ultraviolet and visible absorption spectra of the BTBTHP, the $BiTmO_3$ photocatalyst, and the $BiTmFeSbO_7$ photocatalyst. In order to investigate the band structure of the synthesized samples, we conducted an extensive analysis of the diffuse reflectance absorption spectra of the $BiTmFeSbO_7$ photocatalyst, the $BiTmO_3$ photocatalyst, and the BTBTHP. As depicted in Figure 6a, the absorption edges of the diffuse reflectance spectrum of the $BiTmFeSbO_7$ photocatalyst and the $BiTmO_3$ photocatalyst were detected at 650 nm and 590 nm, respectively. Notably, the BTBTHP displayed a unique shift absorption edge which is located at approximately 685 nm; as a result, the shift absorption edge wavelength of the BTBTHP presented an obvious red shift characteristic compared with that of the $BiTmFeSbO_7$ photocatalyst and the $BiTmO_3$ photocatalyst. The aforesaid phenomenon implied that the BTBTHP possessed a stronger light absorption ability than $BiTmFeSbO_7$ and $BiTmO_3$. Figure 6b shows the correlative diagram of $(\alpha h\nu)^{1/2}$ and $h\nu$ for the synthesized BTBTHP, $BiTmFeSbO_7$, and $BiTmO_3$. Figure 6b further provided a detailed description for the estimated band gap energy of the $BiTmFeSbO_7$ photocatalyst, the $BiTmO_3$ photocatalyst, and the BTBTHP. The calculated band gap energy values of the $BiTmFeSbO_7$ photocatalyst, the $BiTmO_3$ photocatalyst, and the BTBTHP were 1.965 eV, 2.124 eV, and 1.812 eV, respectively. The above band gap energy values are derived from Equation (1) [65]:

$$(\alpha h\nu)^{\frac{1}{2}} = A(h\nu - E_g) \quad (1)$$

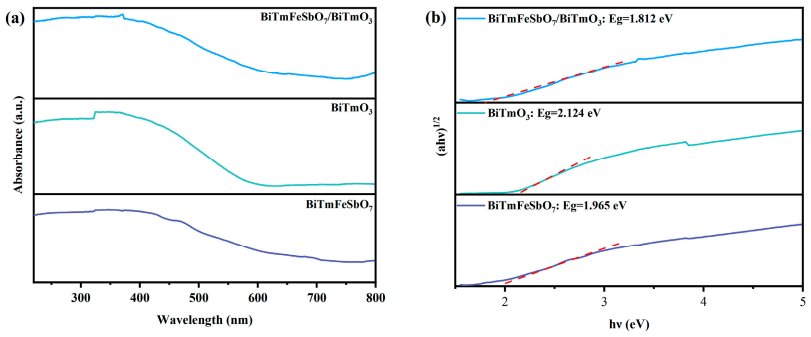


Figure 6. (**a**) The UV–Vis absorption spectra and (**b**) the correlative diagram of $(\alpha h\nu)^{1/2}$ and $h\nu$ of the synthesized BTBTHP, the $BiTmFeSbO_7$ photocatalyst, and the $BiTmO_3$ photocatalyst.

Here, α represents the absorption coefficient, ν represents to the photon energy, A denotes the absorbance factor, and E_g is the band gap energy.

Figure 7a depicts the photoluminescence (PL) spectrum of the $BiTmFeSbO_7$ photocatalyst, the $BiTmO_3$ photocatalyst, and the BTBTHP. Figure 7b displays the time-resolved photoluminescence (TRPL) spectrum of the $BiTmO_3$ photocatalyst. Figure 7c indicates the TRPL spectrum of the $BiTmFeSbO_7$ photocatalyst. Figure 7d shows the TRPL spectrum of the BTBTHP. The photoluminescence spectrum which derived from the $BiTmFeSbO_7$ photocatalyst, the $BiTmO_3$ photocatalyst, and the BTBTHP served as a means to assess the recombination rate of the PEPH and the photodegradation performance. Meanwhile, the TRPL spectra which originated from the $BiTmFeSbO_7$ photocatalyst, the $BiTmO_3$ photocatalyst, and the BTBTHP were capable of providing the electron lifetime of the photocatalyst.

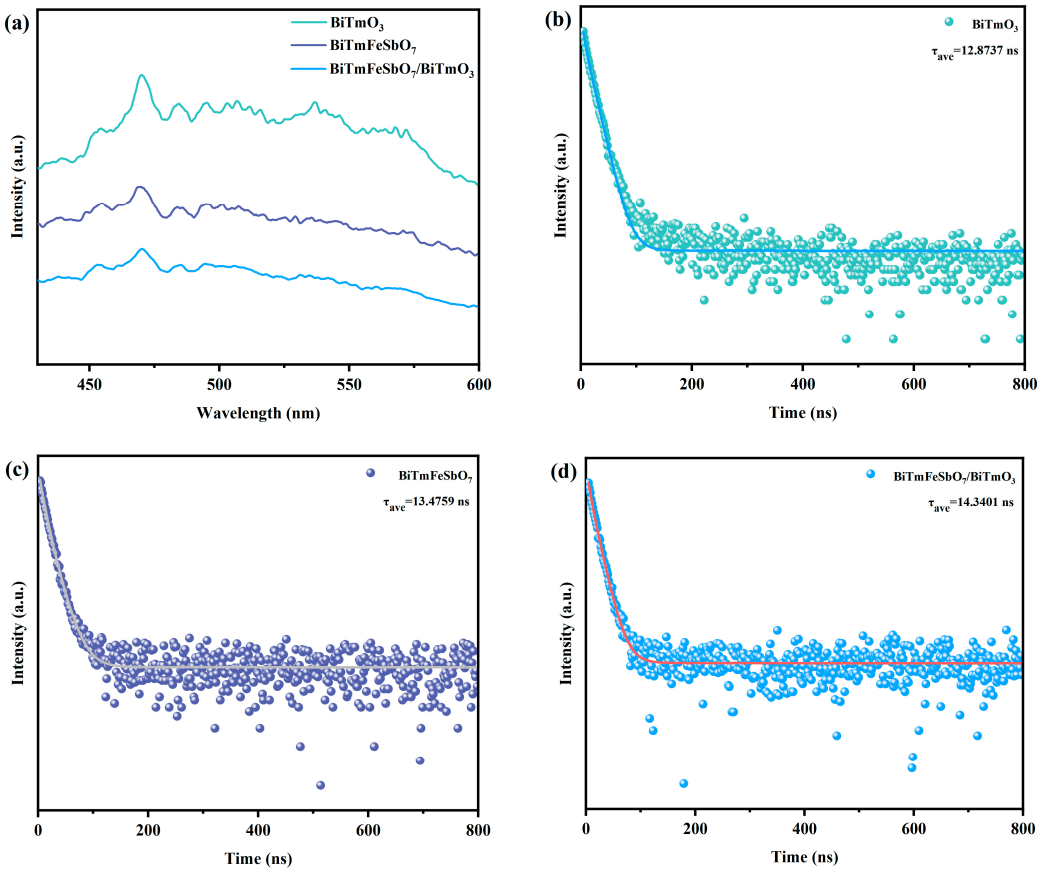


Figure 7. (**a**) The PL spectra of the BTBTHP, the $BiTmFeSbO_7$ photocatalyst, and the $BiTmO_3$ photocatalyst; (**b**) the TRPL spectrum of the $BiTmO_3$ photocatalyst; (**c**) the TRPL spectrum of the $BiTmFeSbO_7$ photocatalyst; (**d**) the TRPL spectrum of the BTBTHP.

Generally, a higher PL intensity implied a faster recombination rate of the PEPH, whereas a lower PL intensity indicated a higher transfer efficiency of the PEPH [66,67]. A relatively high PL intensity was conducive to a decrease in the photocatalytic activity of the $BiTmFeSbO_7$ photocatalyst, the $BiTmO_3$ photocatalyst, and the BTBTHP. As presented in Figure 7a, $BiTmO_3$ exhibited the highest radiation intensity; concurrently, the $BiTmFeSbO_7$ photocatalyst possessed an intermediate radiation intensity between the $BiTmO_3$ photocatalyst and the BTBTHP; ultimately, the BTBTHP owned the lowest radiation intensity. The above experimental result indicated that the separation rate of the PEPH which derived from the BTBTHP was the fastest, and thereby the photocatalytic removal efficiency for degrading the STZ was enhanced by using the BTBTHP. The above

description further demonstrated that the BTBTHP possessed higher photocatalytic activity compared with the $BiTmFeSbO_7$ photocatalyst and the $BiTmO_3$ photocatalyst. The simulative outcomes of the TRPL spectra which were depicted in Figure 7b ($BiTmO_3$), Figure 7c ($BiTmFeSbO_7$), and Figure 7d (BTBTHP) were obtained by employing the double exponential decay Equation (2) [68].

$$I(t) = I_0 + A_1\, exp(-\frac{t}{\tau_1}) + A_2\, exp(-\frac{t}{\tau_2}) \quad (2)$$

In Equation (2) above, A_1 represents the weighting coefficient of the first-order decay times for each decay channel [69], and A_2 represents the weighting coefficient of the second-order decay times for each decay channel [69]. The average lifetime of the PEPH could be computed by using Equation (3) [70].

$$\tau_{ave} = \left(A_1\tau_1^2 + A_2\tau_2^2\right)/(A_1\tau_1 + A_2\tau_2) \quad (3)$$

In accordance with the calculation results, it could be deduced that the lifetime of the BTBTHP (τ_{ave} = 14.3401 ns) was significantly longer than that of the $BiTmFeSbO_7$ photocatalyst (τ_{ave} = 13.4759 ns) and that of the $BiTmO_3$ photocatalyst (τ_{ave} = 12.8737 ns). These results suggest that the BTBTHP exhibits superior photocatalytic activity in comparison with the $BiTmFeSbO_7$ photocatalyst and the $BiTmO_3$ photocatalyst.

Figure 8a presents the photocurrent response spectra of the $BiTmFeSbO_7$ sample, the $BiTmO_3$ sample, and the BTBTHP sample, obtained from the photocurrent experiments. As is evident from Figure 8a, the BTBTHP exhibited the highest intensity of photocurrent response compared with the $BiTmFeSbO_7$ photocatalyst and the $BiTmO_3$ photocatalyst. The above phenomenon suggested that the heterojunction structure which was formed by the $BiTmFeSbO_7$ photocatalyst and the $BiTmO_3$ photocatalyst might facilitate the efficient separation of the PEPH [71,72], and thereby the lifetime of the PEPH was prolonged. Figure 8b displays the Nyquist plots which are obtained from the electrochemical impedance spectroscopy (EIS) measurement experiments. The diameter size value of the semicircle which originates from the mid-frequency region of the Nyquist plot represents the charge transfer resistance (Rct). The Rct reflects the degree of difficulty of the electrochemical reactions which involve electron transfer. A smaller Rct value indicates a greater difficulty for the recombination efficiency of the PEPH and corresponds to a faster electrochemical reaction rate [73,74]. In accordance with the equivalent circuit fitting result, the Rct values of the BTBTHP, the $BiTmFeSbO_7$ photocatalyst, and the $BiTmO_3$ photocatalyst were determined. The Rct values for the BTBTHP, the $BiTmFeSbO_7$ photocatalyst, and the $BiTmO_3$ photocatalyst were 4.63 Ω, 4.86 Ω, and 5.32 Ω, respectively. The experimental results indicated that the descending order of the Rct values for the above three catalysts was BTBTHP < the $BiTmFeSbO_7$ < the BiTmO; obviously, the BTBTHP exhibited the smallest value of the Rct. The above result demonstrated that the electrochemical reaction rate which was facilitated by using the BTBTHP was higher than that by using the $BiTmFeSbO_7$ photocatalyst or the $BiTmO_3$ photocatalyst. Thus, the BTBTHP achieved the highest separation efficiency for the PEPH compared with the $BiTmFeSbO_7$ photocatalyst and the $BiTmO_3$ photocatalyst; as a result, it can be inferred that the BTBTHP possessed higher photocatalytic activity compared with the $BiTmFeSbO_7$ photocatalyst and the $BiTmO_3$ photocatalyst. These photocurrent experimental outcomes are consistent with previous PL experimental results and previous TRPL experimental results, further demonstrating that the BTBTHP possesses superior photocatalytic activity.

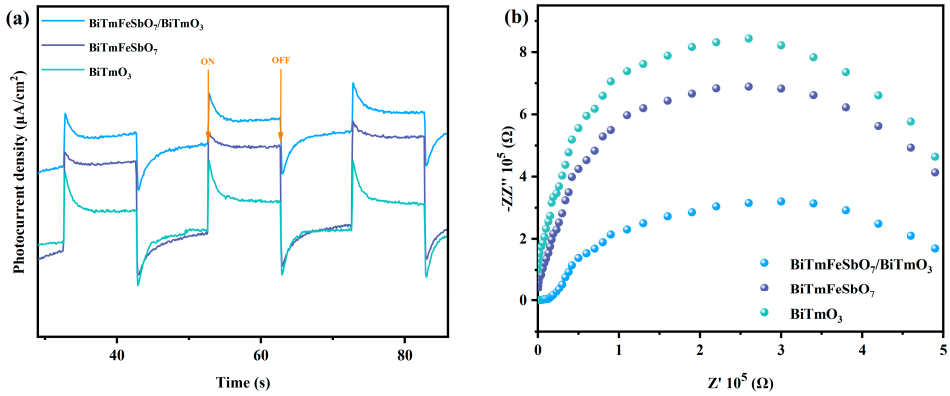


Figure 8. (**a**) The photocurrent density variation curve and (**b**) the EIS plots of the BTBTHP, the $BiTmFeSbO_7$ photocatalyst, and the $BiTmO_3$ photocatalyst.

3.2. Examination of Photocatalytic Degradation Efficiency

3.2.1. Photocatalytic Degradation of the STZ

The photocatalytic performance of the STZ under VLIRN by using the BTBTHP, the $BiTmFeSbO_7$ photocatalyst, the $BiTmO_3$ photocatalyst, and the N-T photocatalyst is depicted in Figure 9. Figure 9a shows the variation curve which is caused by the effect of the STZ concentration on the VLIRN time for the photocatalytic degradation of the STZ by using the BTBTHP, the $BiTmFeSbO_7$ photocatalyst, the $BiTmO_3$ photocatalyst, or the N-T photocatalyst under the condition of VLIRN. The solution was initially stirred in darkness for 45 min to reach adsorption–desorption equilibrium. It can be seen from Figure 9a that the concentration of the STZ gradually decreased with the extension of VLIRN time by using the BTBTHP, the $BiTmFeSbO_7$ photocatalyst, the $BiTmO_3$ photocatalyst, or the N-T photocatalyst. The BTBTHP possessed the highest degradation efficiency for the STZ compared with the $BiTmFeSbO_7$ photocatalyst, the $BiTmO_3$ photocatalyst, or the N-T photocatalyst.

Figure 9b shows the mimetic variation curve which is formed according to the effect of the ln (C_0/C_t) on the VLIRN time during the photocatalytic degradation process of the STZ by using the BTBTHP, the $BiTmFeSbO_7$ photocatalyst, the $BiTmO_3$ photocatalyst, and the N-T photocatalyst. As shown in Figure 9b, the mimetic variation curve caused by the BTBTHP, the $BiTmFeSbO_7$ photocatalyst, the $BiTmO_3$ photocatalyst, and the N-T photocatalyst conformed to the first-order kinetic model. The kinetic constant K_C was calculated using the equation $ln(C_0/C_t) = K_C t$, where C_0 was the initial concentration of the STZ; concurrently, C_t represented the concentration of the STZ at a specific VLIRN time; moreover, t meant the VLIRN time.

Figure 9c summarizes the photodegradation efficiency of the STZ and the kinetic constant K_C after VLIRN of 120 min by using the BTBTHP, the $BiTmFeSbO_7$ photocatalyst, the $BiTmO_3$ photocatalyst, and the N-T photocatalyst. Compared with the $BiTmFeSbO_7$ photocatalyst, the $BiTmO_3$ photocatalyst, and the N-T photocatalyst, BTBTHP had the highest photodegradation efficiency for the STZ. The removal rates of the STZ using the BTBTHP, the $BiTmFeSbO_7$ photocatalyst, the $BiTmO_3$ photocatalyst, and the N-T photocatalyst were 99.50%, 86.91%, 78.00%, and 36.75%, respectively, under the condition of VLIRN. The removal rate of the STZ by using the BTBTHP was 1.14 times that of using the $BiTmFeSbO_7$ photocatalyst, and 1.28 times that of using the $BiTmO_3$ photocatalyst, and 2.71 times that of using the N-T photocatalyst. Furthermore, the reaction rate for degrading the STZ by using the BTBTHP, the $BiTmFeSbO_7$ photocatalyst, the $BiTmO_3$ photocatalyst, or the N-T photocatalyst was 3.87×10^{-9} mol·L^{-1}·s^{-1}, 3.27×10^{-9} mol·L^{-1}·s^{-1}, 2.93×10^{-9} mol·L^{-1}·s^{-1}, or 9.09×10^{-10} mol·L^{-1}·s^{-1}, respectively. The incident photon flux which was obtained after VLIRN was measured to be 4.76×10^{-6} Einstein L^{-1}·s^{-1}

by using a radiometer. In accordance with Equation (4), the photon efficiency (PHE) value for degrading the STZ by using the BTBTHP, the $BiTmFeSbO_7$ photocatalyst, the $BiTmO_3$ photocatalyst, or the N-T photocatalyst was calculated to be 0.0813%, 0.0687%, 0.0615%, or 0.0191%, respectively. The first-order kinetic constant K_C was calculated to be 0.0376 min^{-1}, 0.0128 min^{-1}, 0.0096 min^{-1}, or 0.0026 min^{-1} during the degradation process of the STZ by using the BTBTHP, the $BiTmFeSbO_7$ photocatalyst, the $BiTmO_3$ photocatalyst, or the N-T photocatalyst, respectively. Obviously, the value of the kinetic constant K_C during the degradation process of the STZ by using the BTBTHP was the highest compared with those of using the $BiTmFeSbO_7$ photocatalyst, the $BiTmO_3$ photocatalyst, or the N-T photocatalyst.

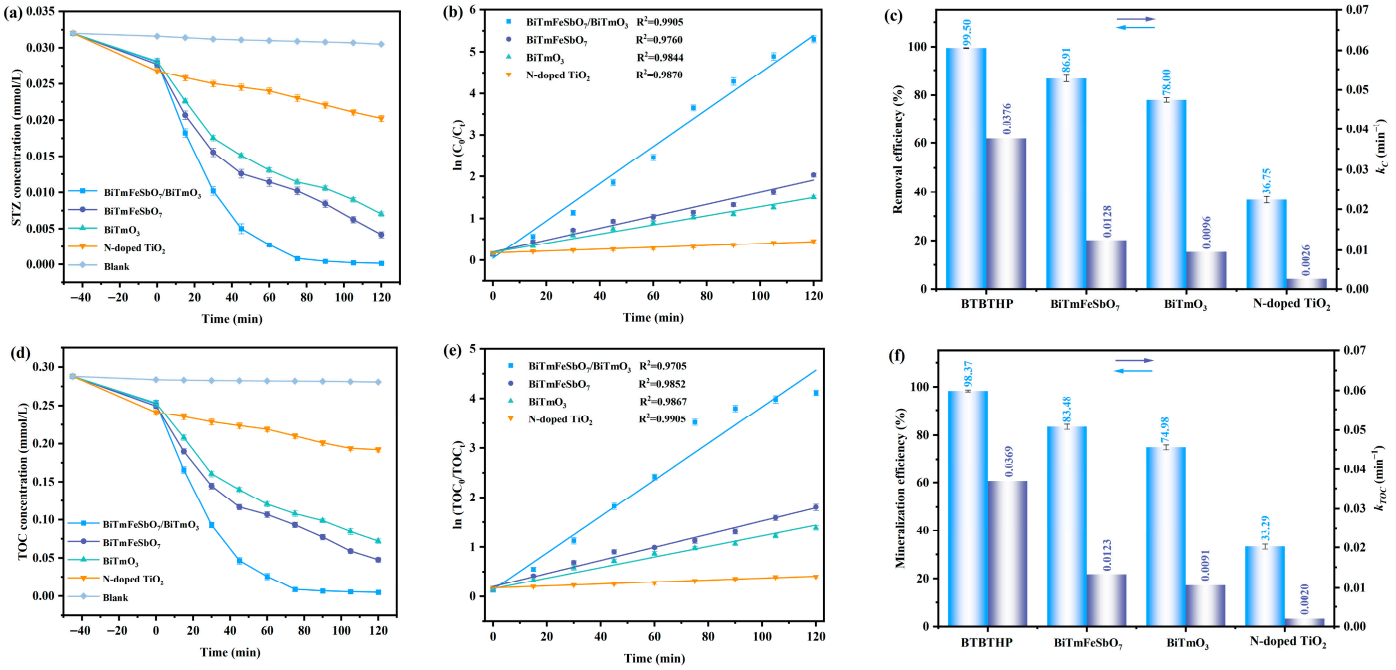


Figure 9. (**a**) The curves of the STZ concentration versus VLIRN time for the photocatalytic degradation of the STZ by using the BTBTHP, the $BiTmFeSbO_7$ photocatalyst, the $BiTmO_3$ photocatalyst, and the N-T photocatalyst; (**b**) The simulative results of $\ln(C_0/C_t)$ versus VLIRN time by using the BTBTHP, the $BiTmFeSbO_7$ photocatalyst, the $BiTmO_3$ photocatalyst, and the N-T photocatalyst; (**c**) The photodegradation rate of the STZ and the kinetic constants after VLIRN of 120 min by using the BTBTHP, the $BiTmFeSbO_7$ photocatalyst, the $BiTmO_3$ photocatalyst, and the N-T photocatalyst; (**d**) The curves of the TOC concentration versus VLIRN time for the photocatalytic degradation of the STZ by using the BTBTHP, the $BiTmFeSbO_7$ photocatalyst, the $BiTmO_3$ photocatalyst, and the N-T photocatalyst; (**e**) The simulative results of the $\ln(TOC_0/TOC_t)$ versus VLIRN time during the degradation process of the STZ by using the BTBTHP, the $BiTmFeSbO_7$ photocatalyst, the $BiTmO_3$ photocatalyst, and the N-T photocatalyst; (**f**) The mineralization efficiency of the TOC concentration and the kinetic constants after VLIRN of 120 min by using the BTBTHP, the $BiTmFeSbO_7$ photocatalyst, the $BiTmO_3$ photocatalyst, and the N-T photocatalyst.

The PHE was calculated according to Equation (4):

$$\phi = R / I_0 \quad (4)$$

As to Equation (4), ϕ represented the photon efficiency; concurrently, R was the degradation rate of the STZ; moreover, I_0 was the photon flux.

Figure 9d shows the variation curve which is formed in accordance with the effect of the total organic carbon (TOC) concentration on the VLIRN time during the photocatalytic degradation process of the STZ by using the BTBTHP, the $BiTmFeSbO_7$ photocatalyst, the $BiTmO_3$ photocatalyst, and the N-T photocatalyst. The results in Figure 9d were consistent

with the degradation results of the STZ. As shown in Figure 9d, the TOC concentration gradually decreased with increasing the VLIRN time; obviously, the BTBTHP exhibited the highest mineralization efficiency for removing the TOC concentration during the photocatalytic degradation process of the STZ compared with the $BiTmFeSbO_7$ photocatalyst, the $BiTmO_3$ photocatalyst, and the N-T photocatalyst.

Figure 9e shows the simulative results of the variation curve which is formed according to the effect of the $\ln(TOC_0/TOC_t)$ on the VLIRN time during the photocatalytic degradation process of the STZ by using the BTBTHP, the $BiTmFeSbO_7$ photocatalyst, the $BiTmO_3$ photocatalyst, and the N-T photocatalyst. It can be found from Figure 9e that the simulative results conformed to the first-order kinetic model. The kinetic constants were calculated by using the equation of $ln(TOC_0/TOC_t) = K_{TOC}t$, where TOC_0 was the initial concentration of TOC; simultaneously, TOC was the reaction concentration of TOC at a specific VLIRN time; in addition, t represented the VLIRN time.

Figure 9f summarizes the mineralization efficiency of TOC concentration and the kinetic constant K_{TOC} during the photocatalytic degradation process of the STZ after VLIRN of 120 min by using the BTBTHP, the $BiTmFeSbO_7$ photocatalyst, the $BiTmO_3$ photocatalyst, and the N-T photocatalyst. The BTBTHP possessed the highest mineralization rate for removing the TOC concentration compared with the $BiTmFeSbO_7$ photocatalyst, the $BiTmO_3$ photocatalyst, and the N-T photocatalyst. In accordance with Figure 9f, the removal rates of the TOC concentration by using the BTBTHP, the $BiTmFeSbO_7$ photocatalyst, the $BiTmO_3$ photocatalyst, and the N-T photocatalyst were 98.37%, 83.48%, 74.98%, and 33.29% after VLIRN of 120 min. The mineralization rate for removing the TOC concentration by using the BTBTHP was 1.18 times that of using the $BiTmFeSbO_7$ photocatalyst, 1.31 times that of using the $BiTmO_3$ photocatalyst, and 2.95 times that of using the N-T photocatalyst. The first-order kinetic constants K_{TOC} were 0.0369 min^{-1}, 0.0123 min^{-1}, 0.0091 min^{-1}, and 0.0020 min^{-1} when the BTBTHP, the $BiTmFeSbO_7$ photocatalyst, the $BiTmO_3$ photocatalyst, and the N-T photocatalyst were utilized for degrading the STZ. Obviously, the value of the kinetic constant K_{TOC} during the photocatalytic degradation process of the STZ by using the BTBTHP was the highest compared with those of using the $BiTmFeSbO_7$ photocatalyst, the $BiTmO_3$ photocatalyst, and the N-T photocatalyst.

In order to evaluate the practical durability and reusability of the synthesized photocatalysts, the cyclic performance tests are conducted by using the synthesized BTBTHP and the results are shown in Figure 10a–f. Figure 10a shows the effect of the STZ concentration on the VLIRN time during quintic cyclic experiments by using the BTBTHP. Figure 10b shows the effect of the $\ln(C_0/C_t)$ on VLIRN time during the quintic cyclic degradation process of the STZ by using the BTBTHP. Figure 10c shows the removal efficiencies of the STZ and the kinetic constants for degrading the STZ during quintic cyclic experiments by using the BTBTHP under the condition of VLIRN. Figure 10d shows the effect of the TOC concentration on the VLIRN time during quintic cyclic experiments by using the BTBTHP. Figure 10e shows the effect of the $\ln(TOC_0/TOC_t)$ on VLIRN time during the quintic cyclic degradation process of the STZ by using the BTBTHP. Figure 10f shows the mineralization efficiency of the TOC concentration and the kinetic constants deriving from the contribution of $\ln(TOC_0/TOC_t)$ and VLIRN time during quintic cyclic experiments by using the BTBTHP. Notably, the BTBTHP exhibited excellent stability during five successive photocatalytic cyclic degradation experiments. Specifically, the degradation efficiency of the STZ by using the BTBTHP after quintic cyclic experiments under the condition of VLIRN was above 94%; concurrently, the mineralization efficiency of the TOC concentration by using the BTBTHP after quintic cyclic experiments under the condition of VLIRN was above 93%. These findings indicated that the BTBTHP possessed significant application potential in the domain of wastewater treatment for removing the STZ pollutant.

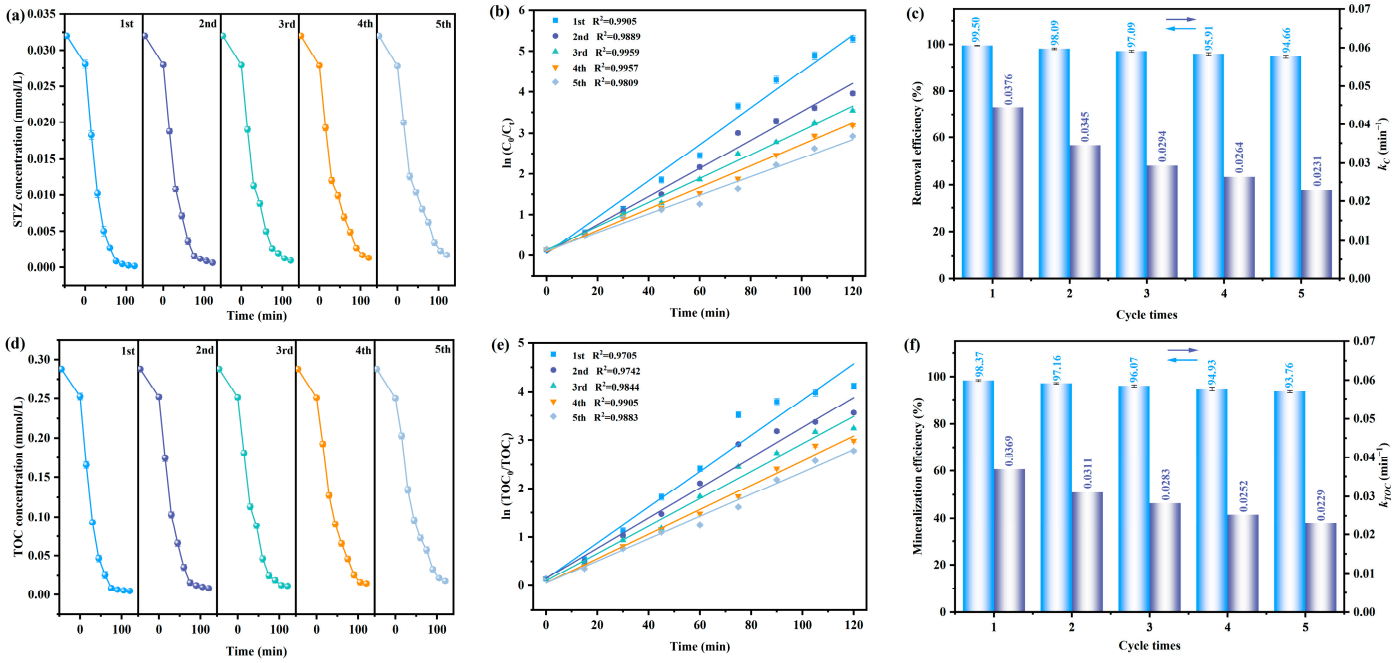


Figure 10. (**a**) The effect of the STZ concentration on the VLIRN time during quintic cyclic experiments by using the BTBTHP; (**b**) The effect of the $\ln(C_0/C_t)$ on VLIRN time during the quintic cyclic degradation process of the STZ by using the BTBTHP; (**c**) The removal efficiencies of the STZ and the kinetic constants for degrading the STZ during quintic cyclic experiments by using the BTBTHP under the condition of VLIRN; (**d**) The effect of the TOC concentration on the VLIRN time during quintic cyclic experiments by using the BTBTHP; (**e**) The effect of the $\ln(TOC_0/TOC_t)$ on VLIRN time during the quintic cyclic degradation process of the STZ by using the BTBTHP; (**f**) The mineralization efficiency of the TOC concentration and the kinetic constants deriving from the contribution of $\ln(TOC_0/TOC_t)$ and VLIRN time during quintic cyclic experiments by using the BTBTHP.

In order to evaluate the structural stability of the BTBTHP, the BTBTHP which was recovered after five cyclical experiments for degrading the STZ was characterized by using the X-ray diffractometer, the ultraviolet and visible spectrophotometer, and the scanning electron microscope. The corresponding results are presented in Figures S11–S14. Figure S11 shows the XRD spectrum of the BTBTHP after the quintic cyclic degradation process of the STZ by using the BTBTHP under the condition of VLIRN. Figure S12 displays the ultraviolet and visible absorption spectrum of the BTBTHP after the quintic cyclic degradation process of the STZ by using the BTBTHP under the condition of VLIRN. Figure S13 indicates the SEM morphology pattern of the BTBTHP after the quintic cyclic degradation process of the STZ by using the BTBTHP under the condition of VLIRN. Figure S14 exhibits the EDS element scanning mapping of the BTBTHP after the quintic cyclic degradation process of the STZ by using the BTBTHP under the condition of VLIRN (Bi, Tm, Fe, Sb, and O from $BiTmFeSbO_7$; simultaneously, Bi, Tm, and O from $BiTmO_3$). As shown in Figure S11, the structure of the BTBTHP remained stable after five consecutive cyclical experiments for degrading the STZ. It can be found from Figure S12 that the ultraviolet and visible absorption spectrum of the recovered BTBTHP did not exhibit significant changes; concurrently, the intrinsic transition absorption edge of the BTBTHP remained unaltered and still situated within the visible light waveband region. Figure S13 indicated that the particle structure of the BTBTHP did not collapse and maintained a perfect crystal texture; meanwhile, the granulometric configuration which derived from the BTBTHP was not changed. Moreover, as shown in Figure S14, the composition content of the BTBTHP was not varied; simultaneously, the metallic simple substance did not precipitate. The molar ratio of the elements which were contained within the recovered

BTBTHP after five consecutive cyclical experiments for degrading the STZ was determined to be Bi:Tm:Fe:Sb:O = 1229:1357:615:621:6158. In conclusion, these results demonstrate that the structure of the BTBTHP remains stable after five consecutive cyclical experiments for degrading the STZ, indicating that the BTBTHP possessed excellent recyclability.

When the initial concentration of the STZ was 0.032 mmol/L, this study investigated the influence of different BTBTHP dosages on the removal efficiency of the STZ during the photocatalytic degradation process of the STZ under the condition of VLIRN. Figure S15 demonstrates the effect of different BTBTHP dosages on the degradation efficiency of the STZ after VLIRN of 120 min. It can be found from Figure S15 that the degradation removal rate of the STZ reached a maximal value of 99.5% when the concentration of the BTBTHP was 0.500 g/L; however, when the concentration of the BTBTHP was further increased, the degradation efficiency of the STZ progressively decreased. The above phenomenon may be attributed to the fact that higher concentrations of the BTBTHP can shield the incident visible light; correspondingly, the accessible surface area for the interactions which occur among visible light, the STZ, and the BTBTHP is reduced; consequently, the utilization efficiency of the active sites which exist on the catalyst surface is decreased.

The initial solution's pH value typically influences the photocatalytic activity of the BTBTHP. Therefore, this study examined the degradation efficiency of the STZ by using the BTBTHP during the photocatalytic degradation process of the STZ under the condition of VLIRN at the initial pH values of 3, 5, 7, 9, or 11. Figure S16 presents the effect of different pH values on the degradation efficiency of the STZ by using the BTBTHP during the photocatalytic degradation process of the STZ under the condition of VLIRN. As shown in Figure S16, the systematic trend for the photocatalytic activity of the BTBTHP was analyzed. The removal rates of the STZ at pH values of 3, 5, 7, 9, and 11 were 91.31%, 93.34%, 99.50%, 96.34%, and 76.42% by using the BTBTHP after VLIRN of 120 min. These results demonstrate that neutral and weakly alkaline conditions are conducive to enhancing the removal rate of the STZ; conversely, the removal rate of the STZ decreased under acidic conditions. Based on the above results, a neutral pH value of 7 was selected as the experimental condition for this study.

In order to investigate the effect of the anion category on the removal rate for the STZ by using the BTBTHP under the condition of VLIRN, ultrapure water which contained four different anions was introduced into the photocatalytic reaction system; meanwhile, every anion possessed a concentration of 10 mmol/L. Figure S17 illustrates the influence of different anions on the degradation efficiency of the STZ during the photocatalytic degradation process of the STZ by using the BTBTHP under the condition of VLIRN. As shown in Figure S17, after the addition of SO_4^{2-}, NO_3^-, Cl^- or CO_3^{2-}, the degradation efficiency of the STZ declined by using the BTBTHP under the condition of VLIRN. After VLIRN of 120 min, the removal rate of the STZ reached 99.5% during the photocatalytic degradation process of the STZ by using the BTBTHP. Under the identical conditions, the introduction of 10 mmol/L SO_4^{2-} into the photocatalytic reaction system resulted in a removal rate of 98.7% for the STZ by using the BTBTHP; moreover, the removal rate of the STZ was 96.9% with the addition of 10 mmol/L NO_3^- by using the BTBTHP under the condition of VLIRN, concurrently, the photodegradation removal rate of the STZ dropped to 60.3% with the augmentation of 10 mmol/L Cl^-, eventually, the degradation removal rate of the STZ was 65.6% with the increment of 10 mmol/L CO_3^{2-}. The aforementioned results indicate that the Cl^- ions which are contained within water sources have a significant impact on the degradation efficiency of the STZ. Higher concentrations of the chloride ion lead to greater consumption of the hydroxyl radicals and the photogenerated holes, ultimately, a reduction in the active radicals is realized in the wastewater system, thereby, the photocatalytic reaction is hindered, finally, a decrease for the removal rate of the STZ is realized. In contrast, water sources which contained high concentrations of SO_4^{2-} and

NO_3^- exhibited a weaker inhibitory effect during the photocatalytic degradation process of the STZ. This is primarily because SO_4^{2-} or NO_3^- only consume the photogenerated holes without affecting the generation of the hydroxyl radicals, thus a lesser inhibition degree for the overall photocatalytic degradation of the STZ appeared.

This study investigated the influence of the initial STZ concentration on the photocatalytic degradation efficiency of the STZ by using the BTBTHP under the condition of VLIRN. Figure S18 demonstrates the effect of different initial STZ concentrations on the degradation efficiency of the STZ by using the BTBTHP under the condition of VLIRN. As shown in Figure S18, when the initial concentrations of the STZ were 0.008 mmol/L, 0.016 mmol/L, 0.032 mmol/L and 0.064 mmol/L, the corresponding degradation efficiencies of the STZ reached 99.63%, 99.57%, 99.50% and 89.65%, respectively. These results indicate that the high initial concentrations of the STZ lead to rapid saturation of the active sites which existed on the BTBTHP surface; meanwhile, the substantial quantity of the generated intermediate products further occupies these active sites, consequently, the continuous generation of the active radicals was hindered. When the BTBTHP was employed under the condition of VLIRN, the degradation reactions proceeded too rapidly for accurate experimental observation at initial STZ concentration of 0.008 mmol/L or 0.016 mmol/L. Therefore, an initial STZ concentration of 0.032 mmol/L was selected as the standard condition for the photocatalytic experiments in this study.

In order to investigate the active substances which were generated during the photodegradation process of the STZ by using the BTBTHP under the condition of VLIRN, the experiments for trapping the radicals were conducted. The hydroxyl radicals (•OH) were captured by using the IPA; concurrently, the superoxide anions ($\bullet O_2^-$) were captured by using the BQ; moreover, the photoinduced holes (h^+) were captured by using the EDTA. Figure 11a shows the change curves which derive from the effect of the STZ concentration on the VLIRN time with the addition of the radical scavengers such as IPA, BQ, and EDTA. Figure 11b shows the removal efficiency of the STZ during the photocatalytic degradation process of the STZ by using the BTBTHP with IPA, BQ, and EDTA as scavengers under the condition of VLIRN. For the sake of eliminating the •OH, the $\bullet O_2^-$, and the h^+ during the photocatalytic degradation process of the STZ, the radical scavengers such as IPA, BQ, and EDTA were introduced at the initial stage of the photodegradation process of the STZ. The results which are displayed in Figure 11a,b indicated that the removal efficiency of the STZ was 99.50% by using the BTBTHP under the condition of VLIRN without using the scavenger; simultaneously, the removal rate of the STZ decreased to 50.38% in the presence of the IPA by using the BTBTHP under the condition of VLIRN; moreover, the removal rate of the STZ decreased to 69.16% in the presence of the BQ by using the BTBTHP under the condition of VLIRN; ultimately, the removal rate of the STZ decreased to 87.94% in the presence of the EDTA by using the BTBTHP under the condition of VLIRN. The above results indicated that $\bullet O_2^-$, •OH, and h^+ could be utilized as reactive radicals for involvement in the photocatalytic degradation of the STZ. The above experimental results demonstrated that the hydroxyl radicals exhibited the strongest oxidative removal capacity for degrading the STZ compared with the superoxide anions and the photoinduced holes during the photocatalytic degradation process of the STZ by using the BTBTHP under the condition of VLIRN. Among the three reactive radicals, the oxidative removal capacity for degrading the STZ decreased in the descending order of •OH > $\bullet O_2^-$ > h^+. Figure 11c shows the electron paramagnetic resonance (EPR) spectrum of the DMPO•O_2^- and the DMPO•OH during the photocatalytic degradation process of the STZ by using the BTBTHP under the condition of VLIRN. As depicted in Figure 11c, after VLIRN for 10 min, the EPR spectrum exhibited a distinct DMPO•OH signal which presented a four lines signal with an intensity ratio of 1:2:2:1 which confirmed the presence of the hydroxyl radicals [75]. Ad-

ditionally, the EPR spectrum displayed a distinct DMPO•O_2^- signal which followed four prominent peaks with an intensity ratio of 1:1:1:1 [75]. The aforementioned experimental results demonstrated that the hydroxyl radicals and the superoxide anions were simultaneously generated during the photodegradation process of the STZ by using the BTBTHP under the condition of VLIRN. The yield of the reactive radicals was determined by the relative intensity of the EPR signals; therefore, it can be concluded that the yield of the hydroxyl radicals was significantly higher than the yield of the superoxide anions [75,76]. The aforementioned experimental results were consistent with the results which originated from the previous radical scavenger experiments; ultimately, it was corroborated that the involvement of the hydroxyl radicals and the superoxide anions during the photocatalytic degradation process of the STZ was realized.

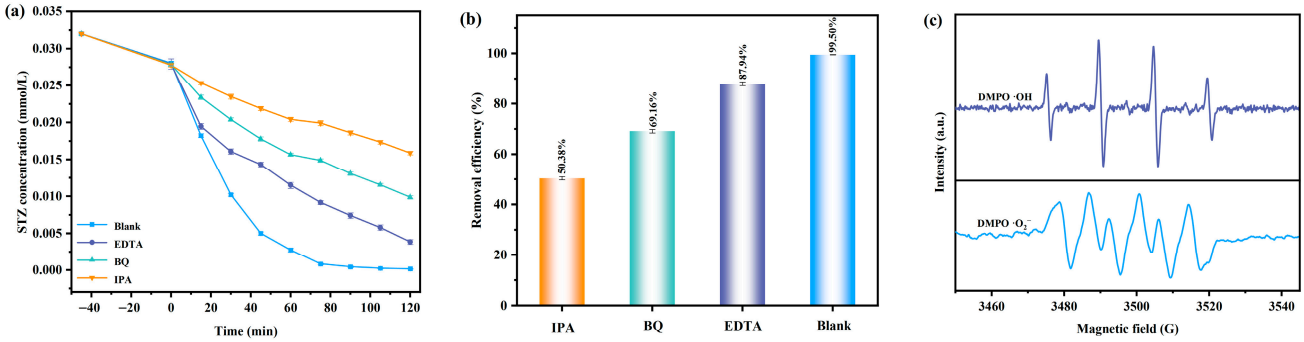


Figure 11. (**a**) The change curves deriving from the effect of the STZ concentration on the VLIRN time with the addition of the radical scavenger such as IPA, BQ, and EDTA; (**b**) The removal efficiency of the STZ during the degradation process of the STZ by using the BTBTHP with IPA, BQ, and EDTA as scavengers under the condition of VLIRN; (**c**) The EPR spectra of DMPO•O_2^- and DMPO•OH during the degradation process of the STZ by using the BTBTHP under the condition of VLIRN.

3.2.2. Comparison of the Photocatalytic Activity

In order to demonstrate the innovative value and application potential of this research, a comprehensive comparative analysis which corresponded to the removal rate of the STZ by using different photocatalysts was conducted. Table 1 displays the comparison results for the photocatalytic activity of the BTBTHP with other reported photocatalysts during the photodegradation process of the STZ under the condition of VLIRN. As systematically summarized in Table 1, the results clearly indicated that the photocatalytic activity of the BTBTHP outperformed that of other photocatalysts significantly. The exceptional effectiveness of the BTBTHP for the photocatalytic degradation of the STZ has been demonstrated under the condition of VLIRN, indicating that the BTBTHP highlighted the superior activity compared with other existing photocatalysts.

Table 1. The comparison results for the photocatalytic activity of the BTBTHP with other reported photocatalysts during the photodegradation process of the STZ under the condition of VLIRN.

Photocatalyst	Incident Light	Irradiation Time (min)	Name of Antibiotic	Removal Rate (%)	Reference
$HTiO_2$-NS	Visible light	360	Sulfathiazole	70	[77]
C_{70}-TiO_2	Visible light	180	Sulfathiazole	90	[78]
DWCNT-N/TiO_2	Visible light	180	Sulfathiazole	77	[79]
CN-0.1Ni/NiOx	Visible light	240	Sulfathiazole	78.5	[80]
YAG:Ce/ZnO 1/1 CSN	Visible light	300	Sulfathiazole	80	[81]
$BiTmFeSbO_7$	Visible light	120	Sulfathiazole	86.91	This study
BTBTHP	Visible light	120	Sulfathiazole	99.50	This study

3.2.3. Possible Photocatalytic Mechanism of the STZ

Figure 12 presents the ultraviolet photoelectron spectrum (UPS) of $BiTmFeSbO_7$ and $BiTmO_3$. The UPS analysis was conducted for determining the ionization potential of $BiTmFeSbO_7$ or $BiTmO_3$ accurately. As depicted in Figure 12, the onset binding energy (Ei) and the cutoff binding energy (Ecutoff) of $BiTmFeSbO_7$ were 0.213 eV and 18.501 eV, respectively; simultaneously, the Ei and the Ecutoff of $BiTmO_3$ were 1.174 eV and 20.846 eV, respectively [82]. According to the excitation energy of 21.2 eV, the valence band (VB) ionization potentials of the $BiTmO_3$ and the $BiTmFeSbO_7$ were ascertained to be 1.528 eV and 2.912 eV, respectively [83,84]. Subsequently, the conduction band (CB) potentials of $BiTmO_3$ and $BiTmFeSbO_7$ were determined to be −0.596 eV and 0.947 eV, respectively.

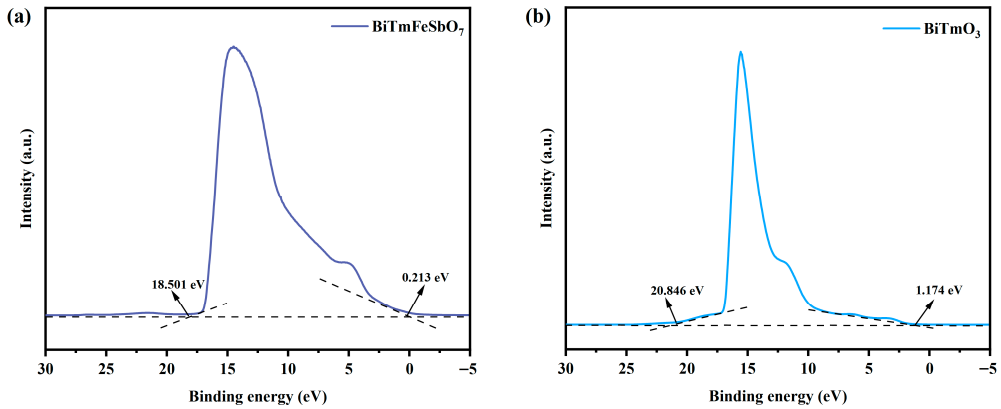


Figure 12. The UPS spectra of (**a**) the $BiTmFeSbO_7$ photocatalyst and (**b**) the $BiTmO_3$ photocatalyst.

After determining the VB ionization potentials of the $BiTmFeSbO_7$ and the $BiTmO_3$, the CB potentials of the $BiTmFeSbO_7$ and the $BiTmO_3$ could be obtained. Concurrently, an in-depth investigation into the photocatalytic mechanism for degrading the STZ by using the BTBTHP was carried out. Consequently, two possible heterojunction photocatalysts were proposed: the conventional type-II heterojunction photocatalyst and the direct Z-scheme heterojunction photocatalyst [85]. Figure 13 exhibits the plausible photodegradation mechanism of the STZ by using the BTBTHP under the condition of VLIRN. As depicted in Figure 13a, in the structure of the conventional type-II heterojunction photocatalyst $BiTmFeSbO_7/BiTmO_3$, owing to the potential difference in the heterojunction photocatalyst $BiTmFeSbO_7/BiTmO_3$, the photogenerated electrons which existed in the CB position of the $BiTmO_3$ would transfer to the CB position of the $BiTmFeSbO_7$; as a result, the photogenerated electrons would accumulate in the CB position of the $BiTmFeSbO_7$; thereby, the reduction potential for the CB position of the $BiTmFeSbO_7$ decreased. Concurrently, the photogenerated holes which resided in the VB position of the $BiTmFeSbO_7$ would migrate to the VB position of the $BiTmO_3$. As a result, the photogenerated holes accumulated in the VB position of the $BiTmO_3$; correspondingly, the oxidation potential for the VB position of the $BiTmO_3$ reduced. In accordance with the above assumption, the CB potential 0.947 eV for $BiTmFeSbO_7$ was more positive than the $O_2/\bullet O_2^-$ potential of −0.33 eV (vs. NHE), and thus the photogenerated electrons which existed in the CB position of the $BiTmFeSbO_7$ could not effectively react with O_2 for generating $\bullet O_2^-$ [86]. Similarly, the negative VB potential value of 1.528 eV for the $BiTmO_3$ was lower than the potential value of 2.38 eV (vs. NHE) which corresponded to ($OH^-/\bullet OH$); as a result, the above result would inhibit the generation of •OH in the VB position of the $BiTmO_3$ [87]. Nevertheless, these findings conflicted with the experimental results of $\bullet O_2^-$ radicals and •OH radicals which were obtained from the trapping radicals experiments and the EPR experiments.

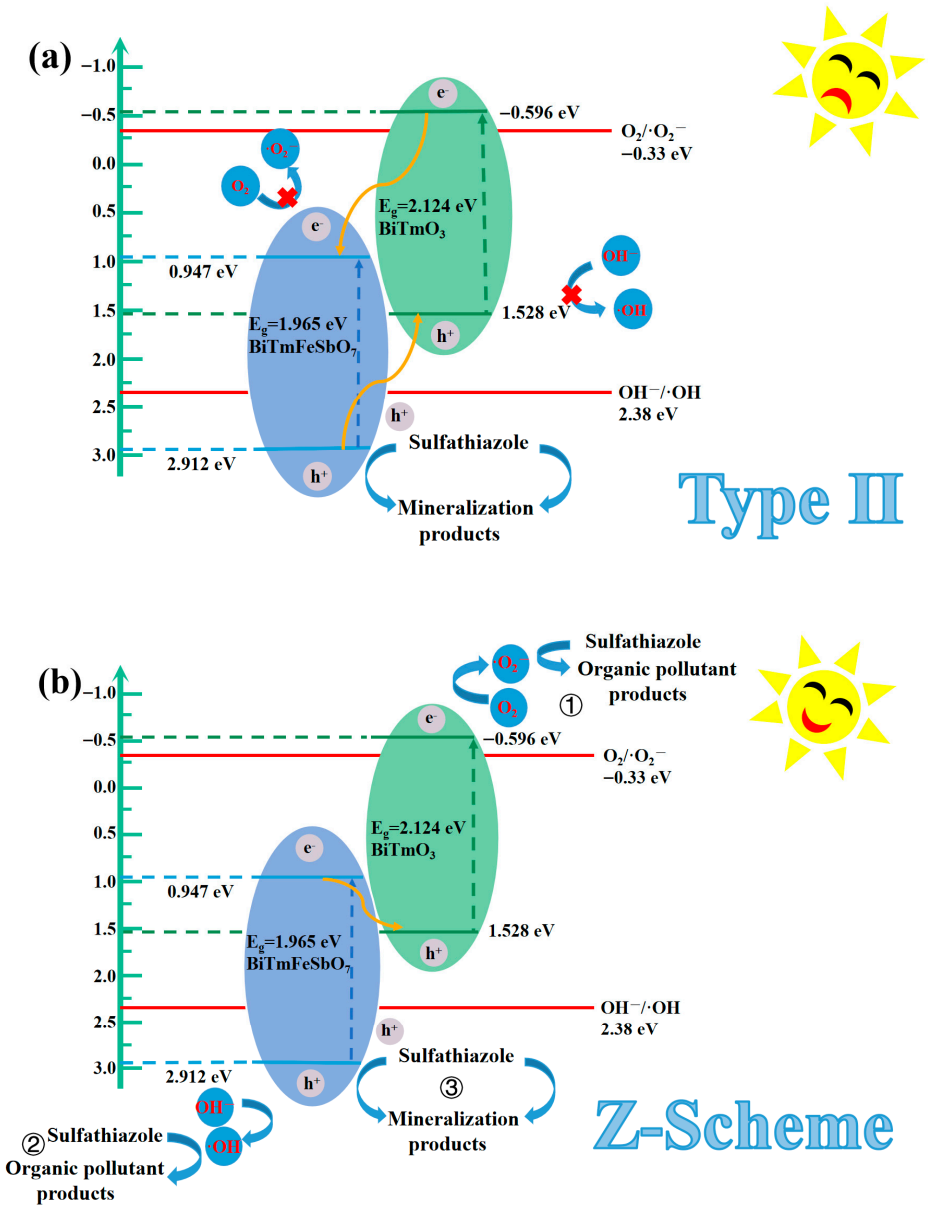


Figure 13. Plausible photodegradation mechanism of the STZ by using the BTBTHP under the condition of VLIRN: (**a**) conventional type II; (**b**) direct Z-scheme.

Based on the foregoing results, we hypothesized that the direct Z-scheme heterojunction provided a reasonable explanation for the photocatalytic degradation mechanism of the STZ with the $BiTmFeSbO_7/BiTmO_3$ heterojunction as the photocatalyst under the condition of VLIRN in this study. Figure 13b presented the Z-scheme heterojunction mechanism for degrading the STZ by using the BTBTHP under the condition of VLIRN. As a result, the photogenerated electrons migrated from the CB position which had a potential of 0.947 eV for $BiTmFeSbO_7$ to the VB which possessed a potential of 1.528 eV for $BiTmO_3$. The above migration process effectively facilitated the separation of the photogenerated electrons and the photogenerated holes; concurrently, high oxidation potential and high reduction potential were maintained; thereby, the high oxidation potential and the high reduction potential were conducive to improving the photocatalytic degradation efficiency of the STZ. Consequently, the structure of the BTBTHP enabled the photoinduced electrons which existed in the CB position of the $BiTmO_3$ to interact with O_2 for generating the $\bullet O_2^-$; thereby, the target pollutant STZ was degraded by using the $\bullet O_2^-$ (① in Figure 13b). Simultaneously, the h^+ which existed in the VB position of the $BiTmFeSbO_7$ reacted with OH^-

for producing the •OH which played a pivotal role during the photocatalytic degradation process of the pollutant STZ (② in Figure 13b). Furthermore, the photogenerated holes (h^+) which existed in the VB position of both $BiTmFeSbO_7$ and $BiTmO_3$ could directly catalyze and oxidize the STZ due to the inherent potent oxidation capacity of the photoinduced holes; subsequently, the photoinduced holes participated in the subsequent degradation process of the STZ (③ in Figure 13b). It was noteworthy that the above analysis results were consistent with the findings which derived from the radical trapping experiments and the EPR experiments, as depicted in Figure 11.

Consequently, the above analysis results reveal that the charge transfer pathway which belongs to the heterojunction which is composed of $BiTmFeSbO_7$ and $BiTmO_3$ follows the direct Z-scheme mechanism under the condition of VLIRN; as a result, the photocatalytic activity of the BTBTHP is enhanced.

3.2.4. Possible Contribution of Each Element for the Photocatalytic Degradation of the STZ

The distortion of lone pair electrons which exist in the bismuth 6s orbital can induce hybridization between the Bi 6s orbital and the O 1s orbital in the valence band of the photocatalyst. This orbital interaction contributes to a decrescence of the band gap width and facilitates the migration rate of the PEPH; therefore, the visible light response capability of the BTBTHP is enhanced [88,89]. Furthermore, the incorporation of the thulium (Tm) element plays a similar role which originates from other rare-earth dopants. The f-f electronic transition within the 4f orbit of the Tm element effectively broadens the light absorption range; thereby, more efficient utilization of the solar light is realized and, simultaneously, the separation efficiency of the PEPH is enhanced [90–92]. The drawing in iron (Fe) element serves as the electron traps and the active sites; therefore, substantial absorption of visible light energy is realized through localized interactions within the photocatalyst. Fe^{3+} ions will function as the trapping centers which can capture and transfer the PEPH; as a result, the recombination probability of the PEPH may be effectively suppressed [93–95]. Meanwhile, the antimony (Sb) element possesses ns^2 electron lone pairs, which significantly enhance charge carrier concentration and promote the formation of the oxygen vacancies; consequently, the photoelectronic properties of the BTBTHP can be improved. The doping of the antimony element achieves a contraction of the optical band gap; as a result, the recombination efficiency of the PEPH may be effectively suppressed [96–98]. Consequently, the above results promote the generation of the hydroxyl radicals and accelerate the overall photocatalytic reaction rate. The formation of a Z-scheme heterojunction which derives from the $BiTmFeSbO_7$ photocatalyst and the $BiTmO_3$ photocatalyst constitutes the key factor for achieving synergistic enhancement. This Z-scheme heterojunction $BiTmFeSbO_7/BiTmO_3$ enables the PEPH to separate effectively; therefore, a great quantity of active species which possess high oxidizing ability is generated during the photocatalytic degradation process of the STZ under the condition of VLIRN; correspondingly, the above active species contains the hydroxyl radicals and the superoxide anions. Consequently, the above mechanism leads to the highly efficient degradation removal rate of the STZ by using the BTBTHP under the condition of VLIRN.

The removal rate of the STZ by using Sb-doped N-T was 48.36% after VLIRN of 120 min. The removal rate of the STZ by using Sb-doped N-T was higher compared with those of using Bi-doped N-T, Tm-doped N-T, and Fe-doped N-T. Therefore, Sb possessed the most superior properties for degrading the STZ compared with Fe, Bi, and Tm under the condition of VLIRN.

3.2.5. Possible Degradation Pathways of the STZ

Figure 14 displays the possible photodegradation pathways for the STZ under the condition of VLIRN by using the BTBTHP. Based on the experimental results which were

accomplished by using the liquid chromatograph–mass spectrometer (LC–MS) and the existing literature, three different potential degradation pathways of the STZ (m/z = 256) were proposed, as shown in Figure 14 [99–102]. In Pathway 1, the amino group which existed on the benzene ring of the STZ was oxidized to a nitro group; as a result, product P1 was generated with m/z = 286. Subsequently, the S-N bond was broken under the attack of the active radicals; thereby, 4-nitrobenzenesulfonic acid P6 (m/z = 204) and 2-aminothiazole P2 (m/z = 100) were generated [99]. In Pathway 2, the S-N bond was broken under the action of the active radicals; as a result, 2-aminothiazole P2 (m/z = 100) and sulfanilic acid P3 (m/z = 174) were produced. The sulfanilic acid P3 (m/z = 174) underwent oxidation effect and deamination, respectively; as a result, 4-nitrobenzenesulfonic acid P6 (m/z = 204) and benzenesulfonic acid P7 (m/z = 159) were generated [100,101]. In Pathway 3, the S-C bond of the STZ was ruptured; as a result, thiazole-2-sulfonamide acid P4 (m/z = 180) and aniline P5 (m/z = 93) were produced. Subsequently, aniline P5 (m/z = 93) underwent hydroxylation; therefore, 4-aminophenol P8 (m/z = 109) and 4-aminobenzene-1,3-diol P9 (m/z = 125) were formed. Then, 4-aminophenol P8 (m/z = 109) further underwent hydroxylation for generating hydroquinone P10 (m/z = 110) [99–101]. The thiazole ring was attacked by the active radicals; as a result, the ring cleavage and the formation of small-molecule organic acids were realized [101,102]. Ultimately, the intermediate organic products which were generated during the photocatalytic degradation process of the STZ were further decomposed on the surface of the photocatalyst for forming the final products which included CO_2, H_2O, SO_4^{2-}, NH_4^+, and NO_3^-.

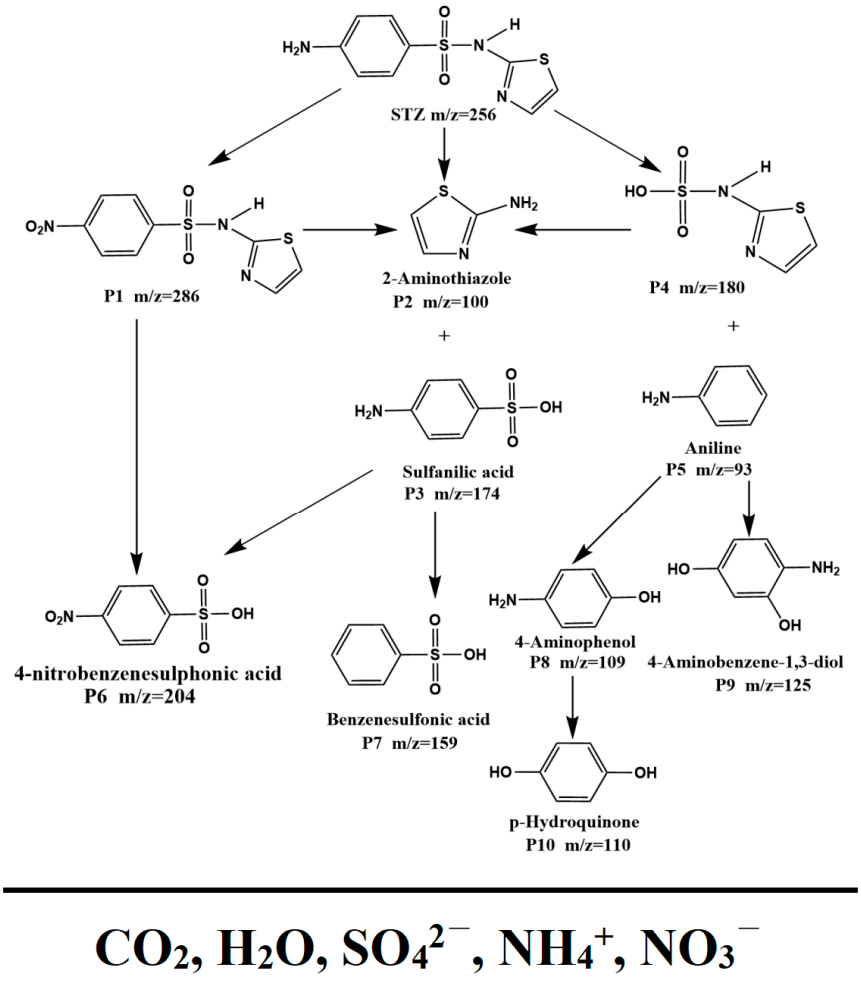


Figure 14. The possible photodegradation pathways for the STZ under the condition of VLIRN by using the BTBTHP.

4. Conclusions

In conclusion, the $BiTmFeSbO_7$ photocatalyst was successfully synthesized by using the solvothermal method for the first time. Meanwhile, the direct Z-scheme BTBTHP was successfully synthesized by means of the ultrasonic-assisted solvothermal method. A Z-scheme heterojunction structure was established between the $BiTmFeSbO_7$ photocatalyst and the $BiTmO_3$ photocatalyst. The BTBTHP which possessed the heterojunction structure significantly enhanced the separation efficiency of the PEPH; concurrently, the BTBTHP maintained a higher redox potential. During the photocatalytic degradation process of the STZ, the BTBTHP demonstrated excellent photocatalytic activity compared with $BiTmFeSbO_7$, $BiTmO_3$, and N-T. Under the condition of VLIRN, the degradation efficiency of the STZ reached as high as 99.5% by using the BTBTHP. Specifically, the degradation rate of the STZ by using the BTBTHP was 1.14 times that of using $BiTmFeSbO_7$, 1.28 times that of using $BiTmO_3$, and 2.71 times that of using N-T. Furthermore, the stability and reusability of the BTBTHP were verified through consecutive cycle degradation experiments. The radical trapping experiments and the EPR analysis results confirmed that $\bullet O_2^-$, •OH, and h^+ were involved in the efficient degradation of the STZ and played a pivotal role during the degradation process of the STZ. In addition, three credible degradation pathways of the STZ were proposed in this study. In summary, the BTBTHP possessed great potential for the treatment of antibiotic-contaminated wastewater. This study provided an effective strategy for treating antibiotic-contaminated wastewater and offered valuable insights into the development of the effective Z-scheme heterojunction photocatalysts.

Supplementary Materials: The following supporting information can be downloaded at https://www.mdpi.com/article/10.3390/nano15231756/s1, Figure S1: The XRD pattern of the $BiTmO_3$ photocatalyst; Figure S2: The XRD pattern of the $BiTmFeSbO_7$ photocatalyst; Figure S3: (a) The XRD pattern and the Rietveld refinement result of the $BiTmFeSbO_7$ photocatalyst and (b) the atomic structure (red atom: O, purple atom: Bi or Tm, light purple atom: Fe or Sb) of the $BiTmFeSbO_7$ photocatalyst; Figure S4: (a) The XRD pattern and the Rietveld refinement result of the $BiTmO_3$ photocatalyst and (b) the atomic structure (red atom: O, purple atom: Bi or Tm) of the $BiTmO_3$ photocatalyst; Figure S5: The XRD spectrum of the N-doped TiO_2 photocatalyst; Figure S6: The Raman spectrum of the $BiTmO_3$ photocatalyst; Figure S7: The Raman spectrum of the $BiTmFeSbO_7$ photocatalyst; Figure S8: The Raman spectrum of the BTBTHP; Figure S9: The TEM morphology image of the BTBTHP; Figure S10: The HRTEM image of the BTBTHP; Figure S11: The XRD spectrum of the BTBTHP after quintic cyclic degradation process of the sulfathiazole by using the BTBTHP under the condition of visible light irradiation; Figure S12: The ultraviolet and visible absorption spectrum of the BTBTHP after quintic cyclic degradation process of the sulfathiazole by using the BTBTHP under the condition of visible light irradiation; Figure S13: The SEM morphology pattern of the BTBTHP after quintic cyclic degradation process of the sulfathiazole by using the BTBTHP under the condition of visible light irradiation; Figure S14: The EDS element scanning mapping of the BTBTHP after quintic cyclic degradation process of the sulfathiazole by using the BTBTHP under the condition of visible light irradiation (Bi, Tm, Fe, Sb, and O from $BiTmFeSbO_7$; simultaneously, Bi, Tm, and O from $BiTmO_3$); Figure S15: The effect of the BTBTHP dosage on the removal efficiency of the STZ; Figure S16: The effect of different pH values on the degradation efficiency of the STZ by using the BTBTHP under the condition of visible light irradiation; Figure S17: The effect of different anions on the degradation efficiency of the STZ by using the BTBTHP under the condition of visible light irradiation; Figure S18: The effect of the initial concentration variation in the STZ on the degradation efficiency of the STZ by using the BTBTHP under the condition of visible light irradiation; Table S1: The removal rates of the STZ by using the $BiTmFeSbO_7/BiTmO_3$ heterojunction photocatalyst with different proportions under the condition of visible light irradiation; Table S2: The atomic characteristic values of the crystal structure of the $BiTmFeSbO_7$ photocatalyst; Table S3: The atomic

characteristic values of the crystal structure for the $BiTmO_3$ photocatalyst; Section S1: Synthesis of Nitrogen-Doped TiO_2; Section S2: Characterization.

Author Contributions: Conceptualization, J.L.; methodology, J.L. and X.G.; software, J.L., X.G., and Y.Y.; validation, J.L., X.G., Y.Y., and L.H.; formal analysis, J.L., X.G., Y.Y., L.H., and M.M.; investigation, J.L., X.G., Y.Y., L.H., and M.M.; resources, J.L. and X.G.; data curation, J.L., X.G., Y.Y., L.H., and M.M.; writing—original draft preparation, J.L., X.G., Y.Y., L.H., and M.M.; writing—review and editing, J.L. and X.G.; visualization, J.L., X.G., and Y.Y.; supervision, J.L.; project administration, J.L.; funding acquisition, J.L. All authors have read and agreed to the published version of the manuscript.

Funding: Funding from the Steeple-Crowned Talent Development Fund of Department of Human Resource and Social Security of Jilin Province of China (Grant No. JiCaiSheZhi [2024] 0451).

Data Availability Statement: The original contributions presented in our study are included in the article/Supplementary Materials. Further inquiries can be directed to the corresponding author(s).

Conflicts of Interest: The authors declare no conflicts of interest.

References

1. Khmaissa, M.; Zouari-Mechichi, H.; Sciara, G.; Record, E.; Mechichi, T. Pollution from livestock farming antibiotics an emerging environmental and human health concern: A review. *J. Hazard. Mater. Adv.* **2024**, *13*, 100410. [CrossRef]
2. Rana, M.S.; Lee, S.Y.; Kang, H.J.; Hur, S.J. Reducing Veterinary Drug Residues in Animal Products: A Review. *FOOD Sci. Anim. Resour.* **2019**, *39*, 687–703. [CrossRef] [PubMed]
3. Zhang, Q.-Q.; Ying, G.-G.; Pan, C.-G.; Liu, Y.-S.; Zhao, J.-L. Comprehensive Evaluation of Antibiotics Emission and Fate in the River Basins of China: Source Analysis, Multimedia Modeling, and Linkage to Bacterial Resistance. *Environ. Sci. Technol.* **2015**, *49*, 6772–6782. [CrossRef] [PubMed]
4. Yang, X.; Chen, Z.; Zhao, W.; Liu, C.; Qian, X.; Zhang, M.; Wei, G.; Khan, E.; Ng, Y.H.; Ok, Y.S. Recent advances in photodegradation of antibiotic residues in water. *Chem. Eng. J.* **2021**, *405*, 126806. [CrossRef]
5. Tzeng, T.W.; Liu, Y.T.; Deng, Y.; Hsieh, Y.C.; Tan, C.C.; Wang, S.L.; Huang, S.T.; Tzou, Y.M. Removal of sulfamethazine antibiotics using cow manure-based carbon adsorbents. *Int. J. Environ. Sci. Technol.* **2016**, *13*, 973–984. [CrossRef]
6. Cai, Z.; Huang, Y.; Ji, H.; Liu, W.; Fu, J.; Sun, X. Type-II surface heterojunction of bismuth-rich $Bi_4O_5Br_2$ on nitrogen-rich g-C_3N_5 nanosheets for efficient photocatalytic degradation of antibiotics. *Sep. Purif. Technol.* **2022**, *280*, 119772. [CrossRef]
7. Deng, W.; Li, N.; Zheng, H.; Lin, H. Occurrence and risk assessment of antibiotics in river water in Hong Kong. *Ecotoxicol. Environ. Saf.* **2016**, *125*, 121–127. [CrossRef]
8. Tong, L.; Huang, S.; Wang, Y.; Liu, H.; Li, M. Occurrence of antibiotics in the aquatic environment of Jianghan Plain, central China. *Sci. Total Environ.* **2014**, *497*, 180–187. [CrossRef]
9. Ou, D.; Chen, B.; Bai, R.; Song, P.; Lin, H. Contamination of sulfonamide antibiotics and sulfamethazine-resistant bacteria in the downstream and estuarine areas of Jiulong River in Southeast China. *Environ. Sci. Pollut. Res.* **2015**, *22*, 12104–12113. [CrossRef]
10. Zhang, R.; Tang, J.; Li, J.; Zheng, Q.; Liu, D.; Chen, Y.; Zou, Y.; Chen, X.; Luo, C.; Zhang, G. Antibiotics in the offshore waters of the Bohai Sea and the Yellow Sea in China: Occurrence, distribution and ecological risks. *Environ. Pollut.* **2013**, *174*, 71–77. [CrossRef]
11. Braschi, I.; Blasioli, S.; Gigli, L.; Gessa, C.E.; Alberti, A.; Martucci, A. Removal of sulfonamide antibiotics from water: Evidence of adsorption into an organophilic zeolite Y by its structural modifications. *J. Hazard. Mater.* **2010**, *178*, 218–225. [CrossRef]
12. Chen, Y.; Jiang, C.; Wang, Y.; Song, R.; Tan, Y.; Yang, Y.; Zhang, Z. Sources, Environmental Fate, and Ecological Risks of Antibiotics in Sediments of Asia's Longest River: A Whole-Basin Investigation. *Environ. Sci. Technol.* **2022**, *56*, 14439–14451. [CrossRef]
13. Patel, M.; Kumar, R.; Kishor, K.; Mlsna, T.; Pittman, C.U., Jr.; Mohan, D. Pharmaceuticals of Emerging Concern in Aquatic Systems: Chemistry, Occurrence, Effects, and Removal Methods. *Chem. Rev.* **2019**, *119*, 3510–3673. [CrossRef] [PubMed]
14. Liao, M.; Su, L.; Deng, Y.; Xiong, S.; Tang, R.; Wu, Z.; Ding, C.; Yang, L.; Gong, D. Strategies to improve WO3-based photocatalysts for wastewater treatment: A review. *J. Mater. Sci.* **2021**, *56*, 14416–14447. [CrossRef]
15. Sun, P.; Liu, Y.; Mo, F.; Wu, M.; Xiao, Y.; Xiao, X.; Wang, W.; Dong, X. Efficient photocatalytic degradation of high-concentration moxifloxacin over dodecyl benzene sulfonate modified graphitic carbon nitride: Enhanced photogenerated charge separation and pollutant enrichment. *J. Clean. Prod.* **2023**, *393*, 136320. [CrossRef]
16. Barrocas, B.T.; Osawa, R.; Oliveira, M.C.; Monteiro, O.C. Enhancing Removal of Pollutants by Combining Photocatalysis and Photo-Fenton Using Co, Fe-Doped Titanate Nanowires. *Materials* **2023**, *16*, 2051. [CrossRef]
17. Rani, B.; Nayak, A.K.; Sahu, N.K. 1—Fundamentals principle of photocatalysis. In *Nanostructured Materials for Visible Light Photocatalysis*; Nayak, A.K., Sahu, N.K., Eds.; Elsevier: Amsterdam, The Netherlands, 2022; pp. 1–22.

18. Kumar, A.; Khan, M.; He, J.; Lo, I.M.C. Recent developments and challenges in practical application of visible-light-driven TiO_2-based heterojunctions for PPCP degradation: A critical review. *Water Res.* **2020**, *170*, 115356. [CrossRef] [PubMed]
19. Dong, W.-X.; Bao, Q.-F.; Gu, X.-Y.; Peng, G.; Zhao, X.-G. $C_3N_4/CaTi_2O_5$ Composite: Synthesis and Photocatalytic Properties. *Chin. J. Inorg. Chem.* **2017**, *33*, 292–298.
20. Li, J.; Han, M.; Guo, Y.; Wang, F.; Sun, C. Fabrication of $FeVO_4/Fe_2TiO_5$ composite catalyst and photocatalytic removal of norfloxacin. *Chem. Eng. J.* **2016**, *298*, 300–308. [CrossRef]
21. Hunge, Y.M.; Yadav, A.A.; Kang, S.-W. Photocatalytic Degradation of Eriochrome Black-T Using $BaWO_4/MoS_2$ Composite. *Catalysts* **2022**, *12*, 1290. [CrossRef]
22. Liu, X.; Huang, L.; Wu, X.; Wang, Z.; Dong, G.; Wang, C.; Liu, Y.; Wang, L. $Bi_2Zr_2O_7$ nanoparticles synthesized by soft-templated sol-gel methods for visible-light-driven catalytic degradation of tetracycline. *Chemosphere* **2018**, *210*, 424–432. [CrossRef]
23. Kaviyarasu, K.; Magdalane, C.M.; Jayakumar, D.; Samson, Y.; Bashir, A.K.H.; Maaza, M.; Letsholathebe, D.; Mahmoud, A.H.; Kennedy, J. High performance of pyrochlore like $Sm_2Ti_2O_7$ heterojunction photocatalyst for efficient degradation of rhodamine-B dye with waste water under visible light irradiation. *J. King Saud Univ. Sci.* **2020**, *32*, 1516–1522. [CrossRef]
24. Gupta, G.; Kansal, S.K.; Umar, A.; Akbar, S. Visible-light driven excellent photocatalytic degradation of ofloxacin antibiotic using $BiFeO_3$ nanoparticles. *Chemosphere* **2023**, *314*, 137611. [CrossRef]
25. Thirumalairajan, S.; Girija, K.; Mastelaro, V.R.; Ponpandian, N. Photocatalytic degradation of organic dyes under visible light irradiation by floral-like $LaFeO_3$ nanostructures comprised of nanosheet petals. *New J. Chem.* **2014**, *38*, 5480–5490. [CrossRef]
26. Zou, Z.G.; Ye, J.H.; Abe, R.; Arakawa, H. Photocatalytic decomposition of water with Bi_2InNbO_7. *Catal. Lett.* **2000**, *68*, 235–239. [CrossRef]
27. Cheng, X.; Guan, R.; Chen, Y.; Qian, Y.; Shang, Q.; Sun, Y. Adsorption and photocatalytic degradation process of oxytetracycline using mesoporous Fe-TiO_2 based on high-resolution mass spectrometry. *Chem. Eng. J.* **2023**, *460*, 141618. [CrossRef]
28. De los Santos, D.M.; Navas, J.; Aguilar, T.; Sanchez-Coronilla, A.; Fernandez-Lorenzo, C.; Alcantara, R.; Carlos Pinero, J.; Blanco, G.; Martin-Calleja, J. Tm-doped TiO_2 and $Tm_2Ti_2O_7$ pyrochlore nanoparticles: Enhancing the photocatalytic activity of rutile with a pyrochlore phase. *Beilstein J. Nanotechnol.* **2015**, *6*, 605–616. [CrossRef] [PubMed]
29. Chen, Z.; Zhang, Z.; Zhong, Z.; Zhang, C.; Xu, J. Preparation and photocatalytic characteristic of Sb-doped anatase TiO_2 powders. *Optoelectron. Adv. Mater. Rapid Commun.* **2011**, *5*, 398–402.
30. Zhang, T.; Sa, G.; Xu, A. Photocatalytic degradation of phenol with one-step hydrothermal synthesized Bi-TiO_2. *Vacuum* **2025**, *233*, 113982. [CrossRef]
31. Alzard, R.H.; Siddig, L.A.; Abdelhamid, A.S.; Ramachandran, T.; Alzamly, A. Structural analysis and photocatalytic activities of bismuth-lanthanide oxide perovskites. *J. Solid State Chem.* **2024**, *329*, 124359. [CrossRef]
32. Li, Y.; Liu, M.; Zhang, M.; Liu, Y.; Zhao, Q.; Li, X.; Zhou, Q.; Chen, Y.; Wang, S. Preparation of g-C_3N_4/TiO_2 Heterojunction Composite Photocatalyst by NaCl Template Method and Its Photocatalytic Performance Enhancement. *Nano* **2023**, *18*, 2350009. [CrossRef]
33. Zhao, C.; Li, Y.; Chu, H.; Pan, X.; Ling, L.; Wang, P.; Fu, H.; Wang, C.-C.; Wang, Z. Construction of direct Z-scheme Bi_5O_7I/UiO-66-NH_2 heterojunction photocatalysts for enhanced degradation of ciprofloxacin: Mechanism insight, pathway analysis and toxicity evaluation. *J. Hazard. Mater.* **2021**, *419*, 126466. [CrossRef]
34. Sepehrmansourie, H.; Alamgholiloo, H.; Pesyan, N.N.; Zolfigol, M.A. A MOF-on-MOF strategy to construct double Z-scheme heterojunction for high-performance photocatalytic degradation. *Appl. Catal. B-Environ. Energy* **2023**, *321*, 122082. [CrossRef]
35. Malefane, M.E.; Mafa, P.J.; Nkambule, T.T.I.; Managa, M.E.; Kuvarega, A.T. Modulation of Z-scheme photocatalysts for pharmaceuticals remediation and pathogen inactivation: Design devotion, concept examination, and developments. *Chem. Eng. J.* **2023**, *452*, 138894. [CrossRef] [PubMed]
36. Liu, K.; Li, J.; Yan, X.; Shi, W.-d. Synthesis of Direct Z-Scheme $MnWO_4$/g-C_3N_4 Photocatalyst with Enhanced Visible Light Photocatalytic Activity. *Nano* **2017**, *12*, 121–130. [CrossRef]
37. Li, H.; Tu, W.; Zhou, Y.; Zou, Z. Z-Scheme Photocatalytic Systems for Promoting Photocatalytic Performance: Recent Progress and Future Challenges. *Adv. Sci.* **2016**, *3*, 1500389. [CrossRef]
38. Tang, Q.-Y.; Luo, X.-L.; Yang, S.-Y.; Xu, Y.-H. Novel Z-scheme $In_2S_3/BiVO_4$ composites with improved visible-light photocatalytic performance and stability for glyphosate degradation. *Sep. Purif. Technol.* **2020**, *248*, 117039. [CrossRef]
39. Mafa, P.J.; Ntsendwana, B.; Mamba, B.B.; Kuvarega, A.T. Visible Light Driven $ZnMoO_4/BiFeWO_6$/rGO Z-Scheme Photocatalyst for the Degradation of Anthraquinonic Dye. *J. Phys. Chem. C* **2019**, *123*, 20605–20616. [CrossRef]
40. Liu, B.; Hu, X.; Yang, J.; Yang, C.; Huang, Y. Construction of direct Z-scheme BiOBr/CuI heterojunction for boosting photocatalytic degradation of phenol. *Catal. Sci. Technol.* **2023**, *13*, 504–515. [CrossRef]
41. Kudo, A.; Kato, H.; Nakagawa, S. Water splitting into H_2 and O_2 on new $Sr_2M_2O_7$ (M = Nb and Ta) photocatalysts with layered perovskite structures: Factors affecting the photocatalytic activity. *J. Phys. Chem. B* **2000**, *104*, 571–575. [CrossRef]
42. Bosca, M.; Pop, L.; Borodi, G.; Pascuta, P.; Culea, E. XRD and FTIR structural investigations of erbium-doped bismuth-lead-silver glasses and glass ceramics. *J. Alloys Compd.* **2009**, *479*, 579–582. [CrossRef]

43. Pascuta, P.; Culea, E. FTIR spectroscopic study of some bismuth germanate glasses containing gadolinium ions. *Mater. Lett.* **2008**, *62*, 4127–4129. [CrossRef]
44. Lu, Z.; Jiang, H.; Yan, P.; Li, J.; Wang, Q. Influences of Tm and N doping on surface properties and photoactivities of anatase-TiO_2 nanoparticles. In *New Materials, Applications and Processes, Pts 1–3*; Trans Tech Publications Ltd.: Baech, Switzerland, 2012; Volume 399–401, pp. 519–526.
45. Kashyap, S.J.; Sankannavar, R.; Madhu, G.M. Iron oxide (Fe_2O_3) synthesized via solution-combustion technique with varying fuel-to-oxidizer ratio: FT-IR, XRD, optical and dielectric characterization. *Mater. Chem. Phys.* **2022**, *286*, 126118. [CrossRef]
46. Kaviyarasu, K.; Sajan, D.; Devarajan, P.A. A rapid and versatile method for solvothermal synthesis of Sb_2O_3 nanocrystals under mild conditions. *Appl. Nanosci.* **2013**, *3*, 529–533. [CrossRef]
47. Rada, S.; Rus, L.; Rada, M.; Zagrai, M.; Culea, E.; Rusu, T. Compositional dependence of structure, optical and electrochemical properties of antimony(III) oxide doped lead glasses and vitroceramics. *Ceram. Int.* **2014**, *40*, 15711–15716. [CrossRef]
48. Janani, B.; Okla, M.K.; Abdel-Maksoud, M.A.; AbdElgawad, H.; Thomas, A.M.; Raju, L.L.; Al-Qahtani, W.H.; Khan, S.S. CuO loaded ZnS nanoflower entrapped on PVA-chitosan matrix for boosted visible light photocatalysis for tetracycline degradation and anti-bacterial application. *J. Environ. Manag.* **2022**, *306*, 114396. [CrossRef]
49. Li, R.; Cai, M.; Xie, Z.; Zhang, Q.; Zeng, Y.; Liu, H.; Liu, G.; Lv, W. Construction of heterostructured $CuFe_2O_4$/g-C_3N_4 nanocomposite as an efficient visible light photocatalyst with peroxydisulfate for the organic oxidation. *Appl. Catal. B-Environ.* **2019**, *244*, 974–982. [CrossRef]
50. Cheng, T.; Gao, H.; Liu, G.; Pu, Z.; Wang, S.; Yi, Z.; Wu, X.; Yang, H. Preparation of core-shell heterojunction photocatalysts by coating CdS nanoparticles onto $Bi_4Ti_3O_{12}$ hierarchical microspheres and their photocatalytic removal of organic pollutants and Cr(VI) ions. *COLLOIDS Surf. A-Physicochem. Eng. Asp.* **2022**, *633*, 127918. [CrossRef]
51. Zhang, S.; Zhang, S.; Song, L. Super-high activity of Bi^{3+} doped Ag_3PO_4 and enhanced photocatalytic mechanism. *Appl. Catal. B-Environ.* **2014**, *152*, 129–139. [CrossRef]
52. Yu, J.; Cui, L.; He, H.; Yan, S.; Hu, Y.; Wu, H. Raman spectra of RE_2O_3 (RE=Eu, Gd, Dy, Ho, Er, Tm, Yb, Lu, Sc and Y): Laser-excited luminescence and trace impurity analysis. *J. Rare Earths* **2014**, *32*, 1–4. [CrossRef]
53. Chahine, A.; Et-tabirou, M.; Pascal, J.L. FTIR and Raman spectra of the Na_2O-CuO-Bi_2O_3-P_2O_5 glasses. *Mater. Lett.* **2004**, *58*, 2776–2780. [CrossRef]
54. Jana, Y.M.; Halder, P.; Ali Biswas, A.; Jana, R.; Mukherjee, G.D. FT-IR and Raman vibrational spectroscopic studies of R_2FeSbO_7 (R^{3+} = Y, Dy, Gd, Bi) pyrochlores. *Vib. Spectrosc.* **2016**, *84*, 74–82. [CrossRef]
55. Maczka, M.; Hanuza, J.; Hermanowicz, K.; Fuentes, A.F.; Matsuhira, K.; Hiroi, Z. Temperature-dependent Raman scattering studies of the geometrically frustrated pyrochlores $Dy_2Ti_2O_7$, $Gd_2Ti_2O_7$ and $Er_2Ti_2O_7$. *J. Raman Spectrosc.* **2008**, *39*, 537–544. [CrossRef]
56. Lei, L.; Li, J.; Zhang, R.; Li, L.; Deng, B.; Zhao, G.; Jin, L.; Li, C.; Zhang, P. Structural phase transitions and their effects on oxygen diffusion in Y_2(Zr1-xTix)$_2O_7$ thin films. *Appl. Phys. A-Mater. Sci. Process.* **2020**, *126*, 1–8. [CrossRef]
57. Moiseyenko, V.N.; Brynza, N.P.; Abu Sal, B.; Holze, R.; Gorelik, V.S.; Sverbil, P.P. Raman Scattering in Nanocomposites Based on Synthetic Opal and Nanocrystalline Bi_2TeO_5. *Inorg. Mater.* **2018**, *54*, 1250–1255. [CrossRef]
58. Irshad, K.A.; Anees, P.; Sahoo, S.; Kumar, N.R.S.; Srihari, V.; Kalavathi, S.; Shekar, N.V.C. Pressure induced structural phase transition in rare earth sesquioxide Tm_2O_3: Experiment and ab initio calculations. *J. Appl. Phys.* **2018**, *124*, 155901. [CrossRef]
59. Su, Q.; Li, J.; Wang, B.; Li, Y.; Hou, L. Direct Z-scheme Bi_2MoO_6/UiO-66-NH_2 heterojunctions for enhanced photocatalytic degradation of ofloxacin and ciprofloxacin under visible light. *Appl. Catal. B-Environ. Energy* **2022**, *318*, 121820. [CrossRef]
60. Liu, B.; Du, J.; Ke, G.; Jia, B.; Huang, Y.; He, H.; Zhou, Y.; Zou, Z. Boosting O_2 Reduction and H_2O Dehydrogenation Kinetics: Surface N-Hydroxymethylation of g-C_3N_4 Photocatalysts for the Efficient Production of H_2O_2. *Adv. Funct. Mater.* **2022**, *32*, 2111125. [CrossRef]
61. Liu, C.; Feng, Y.; Han, Z.; Sun, Y.; Wang, X.; Zhang, Q.; Zou, Z. Z-scheme N-doped $K_4Nb_6O_{17}$/g-C_3N_4 heterojunction with superior visible-light-driven photocatalytic activity for organic pollutant removal and hydrogen production. *Chin. J. Catal.* **2021**, *42*, 164–174. [CrossRef]
62. Wang, L.; Wang, J.; Fei, Y.; Cheng, H.; Pan, H.; Wu, C. Ag_3PO_4/Bi_2WO_6 Heterojunction Photocatalyst with Remarkable Visible-Light-Driven Catalytic Activity. *Crystals* **2023**, *13*, 1531. [CrossRef]
63. Idriss, H. On the wrong assignment of the XPS O1s signal at 531-532 eV attributed to oxygen vacancies in photo- and electro-catalysts for water splitting and other materials applications. *Surf. Sci.* **2021**, *712*, 121894. [CrossRef]
64. Chen, F.-Z.; Li, Y.-J.; Zhou, M.; Gong, X.-X.; Gao, Y.; Cheng, G.; Ren, S.-B.; Han, D.M. Smart multifunctional direct Z-scheme In_2S_3@PCN-224 heterojunction for simultaneous detection and photodegradation towards antibiotic pollutants. *Appl. Catal. B-Environ. Energy* **2023**, *328*, 122517. [CrossRef]
65. Makula, P.; Pacia, M.; Macyk, W. How To Correctly Determine the Band Gap Energy of Modified Semiconductor Photocatalysts Based on UV-Vis Spectra. *J. Phys. Chem. Lett.* **2018**, *9*, 6814–6817. [CrossRef] [PubMed]

66. Ali, T.; Tripathi, P.; Azam, A.; Raza, W.; Ahmed, A.S.; Ahmed, A.; Muneer, M. Photocatalytic performance of Fe-doped TiO_2 nanoparticles under visible-light irradiation. *Mater. Res. Express* **2017**, *4*, 015022. [CrossRef]
67. Balakrishnan, G.; Velavan, R.; Batoo, K.M.; Raslan, E.H. Microstructure, optical and photocatalytic properties of MgO nanoparticles. *Results Phys.* **2020**, *16*, 103013. [CrossRef]
68. Chen, J.; Zhao, X.; Kim, S.-G.; Park, N.-G. Multifunctional Chemical Linker Imidazoleacetic Acid Hydrochloride for 21% Efficient and Stable Planar Perovskite Solar Cells. *Adv. Mater.* **2019**, *31*, 1902902. [CrossRef]
69. Gao, Z.-W.; Wang, Y.; Ouyang, D.; Liu, H.; Huang, Z.; Kim, J.; Choy, W.C.H. Triple Interface Passivation Strategy-Enabled Efficient and Stable Inverted Perovskite Solar Cells. *Small Methods* **2020**, *4*, 2000478. [CrossRef]
70. Chen, J.; Kim, S.-G.; Ren, X.; Jung, H.S.; Park, N.-G. Effect of bidentate and tridentate additives on the photovoltaic performance and stability of perovskite solar cells. *J. Mater. Chem. A* **2019**, *7*, 4977–4987. [CrossRef]
71. Ma, Q.; Kumar, R.K.; Xu, S.-Y.; Koppens, F.H.L.; Song, J.C.W. Photocurrent as a multiphysics diagnostic of quantum materials. *Nat. Rev. Phys.* **2023**, *5*, 170–184. [CrossRef]
72. Cheng, Y.; Ye, J.; Lai, L.; Fang, S.; Guo, D. Ambipolarity Regulation of Deep-UV Photocurrent by Controlling Crystalline Phases in Ga_2O_3 Nanostructure for Switchable Logic Applications. *Adv. Electron. Mater.* **2023**, *9*, 202201216. [CrossRef]
73. Bredar, A.R.C.; Chown, A.L.; Burton, A.R.; Farnum, B.H. Electrochemical Impedance Spectroscopy of Metal Oxide Electrodes for Energy Applications. *ACS Appl. Energy Mater.* **2020**, *3*, 66–98. [CrossRef]
74. Behera, A.; Mansingh, S.; Das, K.K.; Parida, K. Synergistic $ZnFe_2O_4$-carbon allotropes nanocomposite photocatalyst for norfloxacin degradation and Cr (VI) reduction. *J. Colloid Interface Sci.* **2019**, *544*, 96–111. [CrossRef] [PubMed]
75. Zhuang, Y.; Luan, J. Improved photocatalytic property of peony-like InOOH for degrading norfloxacin. *Chem. Eng. J.* **2020**, *382*, 122770. [CrossRef]
76. Dvoranová, D.; Brezová, V.; Mazúr, M.; Malati, M.A. Investigations of metal-doped titanium dioxide photocatalysts. *Appl. Catal. B-Environ.* **2002**, *37*, 91–105. [CrossRef]
77. Gao, Z.; Yang, H.; Mao, J.; Wu, J. Construction of α-Fe_2O_3 and Fe/Co-N_4 structures with faceted TiO_2 nanocrystals for highly efficient degradation of sulfathiazole in water. *J. Clean. Prod.* **2019**, *220*, 668–676. [CrossRef]
78. Wang, S.; Liu, C.; Dai, K.; Cai, P.; Chen, H.; Yang, C.; Huang, Q. Fullerene C_{70}-TiO_2 hybrids with enhanced photocatalytic activity under visible light irradiation. *J. Mater. Chem. A* **2015**, *3*, 21090–21098. [CrossRef]
79. Gao, T.; Liu, Z.; Cheng, F.; Dai, K.; Yang, C.; Chen, H. Preparation of N-Doped Double-Walled Carbon Nanotube-TiO_2 Hybrid with Efficient Visible-Light Photocatalytic Activity via a Two-Step Method. *J. Nanosci. Nanotechnol.* **2017**, *17*, 1510–1516. [CrossRef] [PubMed]
80. Cao, S.; Zhao, Y.; Guo, J.; Fu, M.; Yu, X.; Ren, L.; Chen, H.; Jiang, F. Dual role of nickel acetylacetonate in visible light enhanced hydrogen production and antibiotics degradation of nickel/nickel oxides embedded-graphitic carbon nitrides. *Int. J. Hydrogen Energy* **2024**, *55*, 882–892. [CrossRef]
81. Zammouri, L.; Aboulaich, A.; Capoen, B.; Bouazaoui, M.; Sarakha, M.; Stitou, M.; Mahiou, R. Synthesis of YAG:Ce/ZnO core/shell nanoparticles with enhanced UV-visible and visible light photocatalytic activity and application for the antibiotic removal from aqueous media. *J. Mater. Res.* **2019**, *34*, 1318–1330. [CrossRef]
82. Annadi, A.; Gong, H. Success in both p-type and n-type of a novel transparent AgCuI alloy semiconductor system for homojunction devices. *Appl. Mater. Today* **2020**, *20*, 100703. [CrossRef]
83. Cheng, T.; Gao, H.; Sun, X.; Xian, T.; Wang, S.; Yi, Z.; Liu, G.; Wang, X.; Yang, H. An excellent Z-scheme $Ag_2MoO_4/Bi_4Ti_3O_{12}$ heterojunction photocatalyst: Construction strategy and application in environmental purification. *Adv. Powder Technol.* **2021**, *32*, 951–962. [CrossRef]
84. Xu, S.; Gong, S.; Jiang, H.; Shi, P.; Fan, J.; Xu, Q.; Min, Y. Z-scheme heterojunction through interface engineering for broad spectrum photocatalytic water splitting. *Appl. Catal. B-Environ.* **2020**, *267*, 118661. [CrossRef]
85. Barrocas, B.T.; Ambrozova, N.; Koci, K. Photocatalytic Reduction of Carbon Dioxide on TiO_2 Heterojunction Photocatalysts-A Review. *Materials* **2022**, *15*, 967. [CrossRef]
86. Huang, W.; Li, Y.; Fu, Q.; Chen, M. Fabrication of a novel biochar decorated nano-flower-like MoS_2 nanomaterial for the enhanced photodegradation activity of ciprofloxacin: Performance and mechanism. *Mater. Res. Bull.* **2022**, *147*, 111650. [CrossRef]
87. Yan, S.; Yang, J.; Li, Y.; Jia, X.; Song, H. One-step synthesis of ZnS/BiOBr photocatalyst to enhance photodegradation of tetracycline under full spectral irradiation. *Mater. Lett.* **2020**, *276*, 128232. [CrossRef]
88. Subhiksha, V.; Kokilavani, S.; Khan, S.S. Recent advances in degradation of organic pollutant in aqueous solutions using bismuth based photocatalysts: A review. *Chemosphere* **2022**, *290*, 133228. [CrossRef] [PubMed]
89. Zhou, L.; Song, W.; Chen, Z.; Yin, G. Degradation of Organic Pollutants in Wastewater by Bicarbonate-Activated Hydrogen Peroxide with a Supported Cobalt Catalyst. *Environ. Sci. Technol.* **2013**, *47*, 3833–3839. [CrossRef]
90. Goryacheva, O.A.; Beloglazova, N.V.; Vostrikova, A.M.; Pozharov, M.V.; Sobolev, A.M.; Goryacheva, I.Y. Lanthanide-to-quantum dot Forster resonance energy transfer (FRET): Application for immunoassay. *Talanta* **2017**, *164*, 377–385. [CrossRef]

91. Zhan, W.; Guo, Y.; Gong, X.; Guo, Y.; Wang, Y.; Lu, G. Current status and perspectives of rare earth catalytic materials and catalysis. *Chin. J. Catal.* **2014**, *35*, 1238–1250. [CrossRef]
92. Mikolajczyk, A.; Wyrzykowska, E.; Mazierski, P.; Grzyb, T.; Wei, Z.; Kowalska, E.; Caicedo, P.N.A.; Zaleska-Medynska, A.; Puzyn, T.; Nadolna, J. Visible-light photocatalytic activity of rare-earth-metal-doped TiO_2: Experimental analysis and machine learning for virtual design. *Appl. Catal. B-Environ. Energy* **2024**, *346*, 123744. [CrossRef]
93. Yao, G.-Y.; Liu, Q.-L.; Zhao, Z.-Y. Studied Localized Surface Plasmon Resonance Effects of Au Nanoparticles on TiO_2 by FDTD Simulations. *Catalysts* **2018**, *8*, 236. [CrossRef]
94. Karimi-Maleh, H.; Yola, M.L.; Atar, N.; Orooji, Y.; Karimi, F.; Kumar, P.S.; Rouhi, J.; Baghayeri, M. A novel detection method for organophosphorus insecticide fenamiphos: Molecularly imprinted electrochemical sensor based on core-shell Co_3O_4@MOF-74 nanocomposite. *J. Colloid Interface Sci.* **2021**, *592*, 174–185. [CrossRef]
95. Hui, Y.; Zhang, S. A Facile Synthesis of Fe-doped Zirconium Oxide Nanoparticles for Enhancement of Rhodamine B Dye Degradation. *Int. J. Electrochem. Sci.* **2021**, *16*, 210635. [CrossRef]
96. Kumari, S.S.; Nirmala, W.; Chidhambaram, N.; Prabu, M.; Ganesh, V.; Yahia, I.S. Tuning the physical properties of Sb-doped ZnO nanopowders toward elevated photosensing and photocatalytic activity. *J. Korean Ceram. Soc.* **2023**, *60*, 719–731. [CrossRef]
97. Nasser, R.; Othmen, W.B.H.; Elhouichet, H.; Ferid, M. Preparation, characterization of Sb-doped ZnO nanocrystals and their excellent solar light driven photocatalytic activity. *Appl. Surf. Sci.* **2017**, *393*, 486–495. [CrossRef]
98. Zhang, S.; Zhu, K.; Hu, X.; Peng, R.; Xia, C. Antimony doping to greatly enhance the electrocatalytic performance of $Sr_2Fe_{1.5}Mo_{0.5}O_6$-δ perovskite as a ceramic anode for solid oxide fuel cells. *J. Mater. Chem. A* **2021**, *9*, 24336–24347. [CrossRef]
99. Hu, Z.; Xie, X.; Li, S.; Song, M.; Liang, G.; Zhao, J.; Wang, Z. Rational construct CQDs/BiOCOOH/uCN photocatalyst with excellent photocatalytic performance for degradation of sulfathiazole. *Chem. Eng. J.* **2021**, *404*, 126541. [CrossRef]
100. Zhu, Y.; Qiu, S.; Deng, F.; Zheng, Y.; Li, K.; Ma, F.; Liang, D. Enhanced degradation of sulfathiazole by electro-Fenton process using a novel carbon nitride modified electrode. *Carbon* **2019**, *145*, 321–332. [CrossRef]
101. Deng, F.; Qiu, S.; Olvera-vargas, H.; Zhu, Y.; Gao, W.; Yang, J.; Ma, F. Electrocatalytic sulfathiazole degradation by a novel nickel-foam cathode coated with nitrogen-doped porous carbon. *Electrochim. Acta* **2019**, *297*, 21–30. [CrossRef]
102. Kim, K.-S.; Kam, S.K.; Mok, Y.S. Elucidation of the degradation pathways of sulfonamide antibiotics in a dielectric barrier discharge plasma system. *Chem. Eng. J.* **2015**, *271*, 31–42. [CrossRef]

Disclaimer/Publisher's Note: The statements, opinions and data contained in all publications are solely those of the individual author(s) and contributor(s) and not of MDPI and/or the editor(s). MDPI and/or the editor(s) disclaim responsibility for any injury to people or property resulting from any ideas, methods, instructions or products referred to in the content.